

ORIGINAL ARTICLE

Open Access



COSMIC-2 soundings impacts on a RO-based NOAA microwave satellite data quality monitoring system

Robbie Iacovazzi^{1*} , Quanhua Liu², Xinjia Zhou¹, Stanislav Kireev¹, Ninghai Sun¹ and Shu-peng Ho²

Abstract

The Constellation Observing System for Meteorology, Ionosphere and Climate-2/Formosa Satellite Mission 7 (COSMIC-2) Global Navigation Satellite System (GNSS) Radio Occultation (RO) constellation is the follow-on to the highly successful COSMIC-1 program. The GNSS RO atmospheric soundings have historically been used to generate Community Radiative Transfer Model simulated background (B) microwave (MW) brightness temperature data needed to monitor NOAA operational MW sounding instrument observed (O) antenna temperature (Ta) product quality. This study is motivated by the need to determine the impact of COSMIC-2 RO soundings on this critical long-term monitoring capability. This study is based on individual MW sensor O-B Ta bias (ΔT_a) statistics and "double-difference" inter-sensor Ta bias (δT_a) statistics for two time periods. Time Period 1 (TP1—May 1, 2017, to September 30, 2019) exclusively uses COSMIC-1 and Korea Multi-Purpose Satellite-5 soundings, while Time Period 2 (TP2—October 1, 2019, to December 31, 2020) expands the analysis with COSMIC-2 soundings. The TP1 and TP2 ΔT_a statistics comparisons indicate COSMIC-2 data population augmentation and latitudinal distribution impact the MW sounder performance monitoring tool transition from TP1 to TP2. COSMIC-2 competently supports long-term MW individual sensor and inter-sensor product monitoring for MW radiometer channels with weighting functions that peak between 8 and 30 km. Individual sensor ΔT_a monitoring for other microwave channels that depend on COSMIC-2 data below 8 km and from 30 km to 60 has limitations, but these limitations are shown not to inhibit critical δT_a monitoring.

Keywords: Remote sensing, Joint polar satellite system, Advanced technology microwave sounder, COSMIC-1, COSMIC-2, GNSS radio occultation, Satellite instrument performance monitoring, Community radiative transfer model

1 Introduction

The National Oceanic and Atmospheric Administration (NOAA) operational Advanced Microwave Sounding Unit-A (AMSU-A) and Advanced Technology Microwave Sounder (ATMS) satellite instruments have the unique ability to obtain signals below or deeply into clouds from sun-synchronous low-earth orbit (LEO). This enables them to provide brightness temperature (Tb) data from the surface and different layers of the atmosphere under

all-sky conditions. These data are essential to contemporary numerical weather prediction (NWP), environmental monitoring, and climate change detection. For this reason, microwave (MW) instrument measurement quality tracking and trending are critical for detecting and mitigating sensor performance degradation.

Operational MW sounder data quality monitoring has long been accomplished using radiative transfer model (RTM) simulated background (B) Tb values and observed (O) antenna temperature (Ta) values to formulate O-B Ta bias (ΔT_a) estimates that can be tracked and trended (Weng et al. 2012). To implement this method, atmospheric sounding data, including pressure, temperature, water vapor mixing ratio, and ozone mixing ratio, are

*Correspondence: Robert.Iacovazzi@noaa.gov

¹ GST, Inc., 7501 Greenway Center Drive, Suite 1100, Greenbelt, MD 20770, USA

Full list of author information is available at the end of the article

needed to establish representative internal conditions for the RTM. There are diverse atmospheric sounding sources that can be used to support this method. These include soundings generated from traditional radiosondes, NWP model output, and Global Navigation Satellite System (GNSS) Radio-Occultation (RO).

The Constellation Observing System for Meteorology, Ionosphere, and Climate-1/Formosa Satellite Mission 3 (COSMIC-1/FORMOSAT-3, hereafter COSMIC-1) atmospheric temperature and water vapor soundings have been used to establish internal and boundary conditions for the Community Radiative Transfer Model (CRTM) (Liu and Boukabara 2014) since 2012 for use in the MW sensor data quality monitoring system hosted on the NOAA National Environmental Satellite, Data, and Information Service (NESDIS) Center for Satellite Applications and Research (STAR) Integrated Cal/Val System (ICVS—<https://www.star.nesdis.noaa.gov/icvs/>). A paper describing this system by Iacovazzi et al. (2020) communicated that the GNSS RO data make it possible to monitor the data quality of NOAA operational MW sounding instruments—e.g., NOAA-18 (N18), NOAA-19 (N19), Metop-A (MEA), Metop-B (MEB), and Metop-C (MEC) AMSU-A and S-NPP (NPP) and NOAA-20 (N20) ATMS. The study also elucidated how information from the MW instrument monitoring system are used to support instrument anomaly detection and root cause analysis. After the study was published, Korea Multi-Purpose Satellite-5 (KOMPSAT-5) atmospheric sounding data from its Atmospheric Occultation and Precision Orbit Determination (AOPOD) instrument were added to the monitoring analysis to bolster the flagging COSMIC-1 data sampling population.

The COSMIC-2 mission succeeded in multiple atmospheric and space weather science subdisciplines. For example, Ho et al. (2017) have demonstrated that COSMIC-1 RO temperature data in the lower stratosphere are beneficial to identify the temperature radiative biases for several Rawinsonde Observation (RAOB) sensor types. COSMIC-1 data can be used as an anchor reference to calibrate other satellite data (Ho et al. 2009). More COSMIC-1 science applications for climate and meteorology studies are documented in numerous publications (Ho et al. 2013, 2015, 2018; Huang et al. 2013; Teng et al. 2013; Biondi et al. 2012, 2013; Scherlin-Pirscher et al. 2012; Zeng et al. 2012; Rieckh et al. 2017; Schröder et al. 2019; Xue et al. 2018; Mears et al. 2019, 2020). It is accomplishments such as these that established the need for further GNSS RO missions.

The COSMIC-2/Formosa-7 program, hereafter referred to as COSMIC-2, is the much-needed follow-on to COSMIC-1. On June 25, 2019, six COSMIC-2 microsatellites were launched into LEO on a single SpaceX

Falcon Heavy rocket from Cape Canaveral, Florida. Each microsatellite has an orbital inclination of 24°, which covers 45°S to 45°N and confines most of the soundings between 35°S to 35°N. COSMIC-2 atmospheric temperature and moisture sounding data, computed from atmospheric refractivity measurements and models that establish an initial sounding estimate, are available from October 1, 2019. At the NOAA/NESDIS/STAR, these COSMIC-2 soundings are being used to continue NOAA operational MW sounder monitoring (Ho et al. 2021; Shao et al. 2021). Ho et al. (2020, 2021) have quantified the COSMIC-2 data quality, including their precision, accuracy, and long-term stability. They show COSMIC-2 data shall also be suitable as an anchor reference to calibrate other satellite data just as COSMIC-1 (see Ho et al. 2009) data has been for in-situ RAOB data (see Ho et al. 2017).

In this paper, we determine the COSMIC-2 RO soundings impacts on a heritage NOAA MW sounder data quality monitoring system that has been successful using predecessor GNSS RO soundings. The impacts are deduced from monitoring system results changes analyzed between a period when the system utilized only COSMIC-1 and KOMPSAT-5 GNSS RO sounding data and a later period when the system began harnessing COSMIC-1, KOMPSAT-5, and COSMIC-2 data. Section 2 briefly describes the data used, while Sect. 3 explains the method. Section 4 contains the results illuminating the ΔT_a and δT_a statistical changes between the two analysis periods described above. Section 5 offers a summary of the findings.

2 Observations

Section 2.1 offers overviews of the AMSU-A/ATMS instruments and the common sounding channels between them that are selected for this study. Section 2.2 describes the nature of the GNSS RO observations and their associated atmospheric soundings. When blended with the surface and upper atmosphere portions of the ECMWF Integrated Forecast System 51-member Ensemble (ENS) forecast, the GNSS RO soundings form the basis of most of the atmospheric sounding inputs needed by the CRTM. Note that the ECMWF ENS is run every 6 h out to 15 days with a horizontal resolution of 18 km and 91 layers in the vertical.

2.1 AMSU-A and ATMS microwave radiometer instrument overviews

Space-based passive microwave remote sensing of atmospheric thermal and water vapor structure takes advantage of O₂ and H₂O absorption bands between 23 to 183 GHz (Iacovazzi et al. 2020). There is a very strong O₂ absorption band at 60 GHz and a weaker one at

about 118 GHz. There are three H₂O absorption bands at 23 GHz, 118 GHz, and 183 GHz that increase in strength from low to high frequency. Equally important is that in between these strong absorption bands are spectral regions of weaker absorption that facilitate remote sensing of the surface through clouds.

The NOAA AMSU-A/MHS (Microwave Humidity Sounder) and ATMS operational microwave sounding instruments have several channels. These channels are designed to take advantage of the microwave spectrum absorption properties to perform all-sky atmospheric sounding and surface remote sensing. In addition, most of these channels are specified to be exactly the same or to contain only slight variations between instruments to promote Tb measurement continuity between satellite missions. Critical design characteristics of ATMS and AMSU-A/MHS are listed in Table 1. In Table 1, the radiometer channel weighting function peak altitude, defined as the altitude where the maximum change of transmittance with height occurs, sometimes has a value of “window.” This “window” value represents channels that have their weighting function peak at the surface. This translates to the signal reaching the radiometer

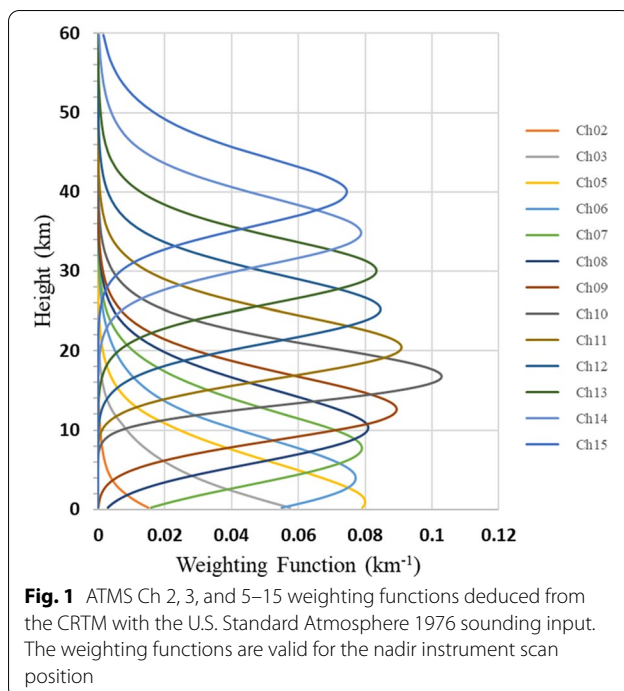
being composed mainly of surface radiation transmitted through the whole atmosphere. The microwave weighting functions for ATMS channels 2, 3, and 5–15—i.e., those scrutinized in the NOAA operational MW sounding instrument data quality monitoring system—have been deduced from the CRTM and plotted in Fig. 1. The weighting functions seen in this figure are generated with the CRTM based on the U.S. Standard Atmosphere 1976 input sounding. The AMSU-A has equivalent bands in Chs 2–14, as documented in Table 1.

The AMSU-A/MHS together represent the predecessor of the ATMS instrument. Thirteen of the 15 AMSU-A channels – the Ka-band Channel (Ch) 2 window at 31.4 GHz and the V-band Chs 3–14 sounding bands from 50.3 GHz to 57.29 GHz—are evaluated by the NOAA/NESDIS/STAR operational RO-based MW sounding instrument data quality monitoring system. The MHS channels and their associated ATMS channels are not monitored by this system, so the nature of these channels is not described here. The AMSU-A satellite radiometer was designed to replace the 4-channel Microwave Sounding Unit (MSU), which was flown on several Polar-orbiting Operational Environmental Satellite

Table 1 Channel number, center frequency, bandwidth, polarization, and nominal beamwidth characteristics of ATMS and AMSU-A/MHS channels and their weighting function peak at nadir for a U.S. Standard Atmosphere 1976 condition

Ch #	Center frequency [GHz]	Bandwidth required/true [GHz]	Polarization	Nominal beamwidth [deg]	Weighting function peak [km]
1	23.8	0.27/1 × 0.27	QV	5.2 (3.3)	Window
2	31.4	0.18/1 × 0.18	QV	5.2 (3.3)	Window
3	50.3	0.18/1 × 0.18	QH (QV)	2.2 (3.3)	Window
4 (N/A)	51.76 (N/A)	0.40 (N/A)/1 × 0.40	QH (N/A)	2.2 (N/A)	0.2 (N/A)
5 (4)	52.8	0.40/1 × 0.40	QH (QV)	2.2 (3.3)	1.4
6 (5)	53.596 ± 0.115	0.17/2 × 0.17	QH	2.2 (3.3)	3.9
7 (6)	54.4	0.40/1 × 0.40	QH	2.2 (3.3)	8.2
8 (7)	54.94	0.40/1 × 0.40	QH (QV)	2.2 (3.3)	11.0
9 (8)	55.5	0.33/1 × 0.33	QH	2.2 (3.3)	12.8
10 (9)	57.29	0.33/2 × 0.155	QH	2.2 (3.3)	16.8
11 (10)	57.29 ± 0.217	0.078/2 × 0.078	QH	2.2 (3.3)	20.9
12 (11)	57.29 ± 0.322 ± 0.048	0.036/4 × 0.036	QH	2.2 (3.3)	25.4
13 (12)	57.29 ± 0.322 ± 0.022	0.016/4 × 0.016	QH	2.2 (3.3)	30.3
14 (13)	57.29 ± 0.322 ± 0.010	0.008/4 × 0.008	QH	2.2 (3.3)	35.4
15 (14)	57.29 ± 0.322 ± 0.0045	0.003/4 × 0.003	QH	2.2 (3.3)	39.4
16 (15/H1)	88.2 (89)	2.0/1 × 2.0	QV	2.2 (3.3/1.1)	Window
17 (H2)	165.5 (157)	3.0/1 × 1.150	QH(QV)	1.1	Window
18 (H5)	183.31 ± 7.0 (190.3)	2.0/1 × 2.0	QH(QV)	1.1	2.1
19 (N/A)	183.31 ± 4.5 (N/A)	2.0 (N/A)/1 × 2.0	QH (N/A)	1.1 (N/A)	3.4 (N/A)
20 (H4)	183.31 ± 3.0	1.0/1 × 1.0	QH	1.1	4.4
21 (N/A)	183.31 ± 1.8 (N/A)	1.0 (N/A)/1 × 1.0	QH (N/A)	1.1 (N/A)	6.4 (N/A)
22 (H3)	183.31 ± 1.0	0.5/1 × 0.5	QH	1.1	7.9

The information about AMSU-A/MHS is added in parenthesis, but only if it is different from ATMS. The term N/A means “not applicable”



(POES) missions since 1978. Table 1 shows that AMSU-A Chs 4–14 have peak weighting functions at different altitudes to allow atmospheric temperature sounding. AMSU-A Chs 2, 3, and 15 are atmospheric window channels with varying amounts of water vapor absorption to allow water vapor content and precipitation estimation. A nominal beamwidth, or the size of the region where 50% of the MW energy is coming from in a given scene, is 3.3° , which leads to a nadir footprint or field-of-view (FOV) size of nearly 50 km. The AMSU-A instrument step-scans $\pm 48.33^\circ$ from nadir to complete a total of 30 individual FOV measurements along scan lines, which leads to a swath width of 2243 km.

The ATMS is a 22-channel cross-track scanning MW radiometer that is manifested on the NPP and N20 satellites. The ATMS instrument's first 15 channels share the same central frequencies as AMSU-A, except ATMS Ch 4 is a 51.7 GHz channel that does not exist on AMSU-A. The ATMS K/Ka-band Chs 1 and 2 have a nominal beamwidth of 5.2° , which leads to a 75 km nadir footprint. The ATMS V-band Chs 3–15 have a nominal beamwidth of 2.2° that equates to a 32 km footprint at nadir. The ATMS instrument scans $\pm 52.725^\circ$ from nadir to complete 96 individual FOV measurements along scan lines. The ATMS has a swath width of 2700 km, which leaves almost no data gap even near the Equator. A crucial architectural change between ATMS Chs 3, 5, and 8 and AMSU-A Chs 3, 4, and 7 is that the polarization is vertical for ATMS and horizontal for AMSU-A. Only the

Table 2 Channel number, center frequency, accuracy, and NEDT specifications for ATMS and AMSU-A/MHS channels

Ch #	Center frequency [GHz]	Accuracy [K]	NEDT @ 300 K [K]
1	23.8	1.0 (2.0)	0.7 (0.3)
2	31.4	1.0 (2.0)	0.8 (0.3)
3	50.3	0.75 (1.5)	0.9 (0.4)
4 (N/A)	51.76 (N/A)	0.75 (N/A)	0.7 (N/A)
5 (4)	52.8	0.75 (1.5)	0.7 (0.25)
6 (5)	53.596 ± 0.115	0.75 (1.5)	0.7 (0.25)
7 (6)	54.4	0.75 (1.5)	0.7 (0.25)
8 (7)	54.94	0.75 (1.5)	0.7 (0.25)
9 (8)	55.5	0.75 (1.5)	0.7 (0.25)
10 (9)	57.29	0.75 (1.5)	0.75 (0.25)
11 (10)	57.29 ± 0.217	0.75 (1.5)	1.2 (0.4)
12 (11)	$57.29 \pm 0.322 \pm 0.048$	0.75 (1.5)	1.2 (0.4)
13 (12)	$57.29 \pm 0.322 \pm 0.022$	0.75 (1.5)	1.5 (0.6)
14 (13)	$57.29 \pm 0.322 \pm 0.010$	0.75 (1.5)	2.4 (0.8)
15 (14)	$57.29 \pm 0.322 \pm 0.0045$	0.75 (1.5)	3.6 (1.2)

The information about AMSU-A/MHS is added in parenthesis, but only if it is different from ATMS. The term N/A means “not applicable”

ATMS Ka-band Ch 2 and V-band Chs 3 and 5–15 are the focus of this study, since they are tracked by the NOAA/NESDIS/STAR monitoring system.

On-board calibration of total power MW sounding radiometers, such as AMSU-A and ATMS, is achieved by observing cold space and a well-characterized internal warm load (blackbody) target during each revolution of the scan reflector antenna. A typical two-point calibration algorithm is carried out using views of cold space and the blackbody. Pre-launch characterized non-linearity is also applied in the calibration. Post-launch data acquired during the Post-launch Test (PLT) period may be used for the calibration. For ATMS, the reflector emissivity derived from the PLT pitch maneuver data is used to correct for antenna reflector emission. This reflector emission correction was implemented into ATMS operational data processing starting on October 15, 2019.

The AMSU-A required measurement accuracy for Chs 1, 2, and 15 is 2.0 K, and for Chs 3–14 is 1.5 K. The ATMS accuracy specification is 50% tighter, with Chs 1 and 2 being 1.0 K and Chs 3–15 being 0.75 K. The noise equivalent delta temperature (NEDT) specification for AMSU-A Chs 1–9 is between 0.25 K and 0.4 K, while for ATMS Chs 1–10 is between 0.7 K to 0.9 K. The NEDT for AMSU-A Chs 10–14 ranges from 0.4 K to 1.2 K, and for ATMS Chs 11–15 spans from 1.2 K to 3.6 K. These values can be found in Table 2. However, there are 96 ATMS samples versus 30 AMSU-A samples per scan and 3 ATMS scan lines compared to a single AMSU-A scan line within the same observation time interval. At the

numerical weather prediction centers, the ATMS noise is effectively reduced by a factor of 3 with help from an ATMS data remapping technique. More information about ATMS and AMSU-A instrument characteristics and calibration is readily available in technical memos and journal articles (Weng et al. 2012, 2013; Han et al. 2016; Yang et al. 2021).

2.2 COSMIC-1 and COSMIC-2 GNSS RO temperature and water vapor soundings overview

Refractivity is a function of temperature, water vapor, and pressure in the neutral atmosphere (Bean and Dutton 1966), and is expressed as

$$N = 77.6 \frac{P}{T} + 3.73 \times 10^5 \frac{P_w}{T^2},$$

where N is refractivity, P is pressure, T is the temperature, and the P_w is the partial pressure of water vapor. Note that in the atmospheric data regions between 8 and 30 km, where there is very little water vapor and gaseous molecular ionization, the refractivity information is mainly contributed from temperature. Below 8 km, RO refractivity information is mainly contributed from both temperature and water vapor concentration, which contributes to larger uncertainty. Above 35 km, refractivity will be affected by both temperature and ionosphere density distribution. Because ionosphere density profiles are very difficult to retrieve, the temperature retrievals above 35 km altitude are of larger uncertainty.

The present study uses the COSMIC Data Analysis and Archive Center (CDAAC) COSMIC-1 and KOMPSAT-5 wetPrf retrieval products to support CRTM MW sounder Tb simulation for the MW radiometer monitoring software. The University Center for Atmospheric Research wetPrf product is retrieved using a one-dimensional variational data assimilation (1D-Var) algorithm (Healy and Eyre 2000; Palmer et al. 2000). A brief description of the 1D-Var algorithm used for COSMIC-1 and KOMPSAT-5 wetPrf sounding retrieval is provided at the CDAAC web site (<https://cdaac-www.cosmic.ucar.edu/cdaac/doc/overview.html>).

The STAR COSMIC-2 wetPrf retrieval products are also used to support the MW radiometer monitoring software. A brief description of the 1D-Var algorithm applied for COSMIC-2 wetPrf sounding retrieval is provided in a poster by Kireev et al. (2020). It is important to note that the CDAAC 1D-Var algorithm used to produce the COSMIC-1 and KOMPSAT-5 wetPrf products and NOAA/NESDIS/STAR 1D-Var algorithm used to produce the COSMIC-2 wetPrf products are compatible.

The COSMIC-1 satellite system consisted of six LEO microsattellites and was launched on April 15, 2006. The perigee and apogee of these LEO satellites are about

770 km and 830 km above the Earth's surface, respectively, and have an orbital inclination angle of 72°. COSMIC-2 similarly is a constellation of six LEO microsattellites, but the perigee and apogee of their orbits are respectively about 530 km and 551 km, and its orbital inclination is only 24°. The orbital inclination represents an impactful difference between COSMIC-1 and COSMIC-2, in that the latitudinal extent of observations of COSMIC-2 is about 45°S to 45°N, while COSMIC-1 data is distributed over the entire globe. Meanwhile, KOMPSAT-5 has a single GNSS RO receiver with an orbital perigee and apogee of about 559 km and 562 km, respectively, and a 97.6° orbital inclination. Thus, KOMPSAT-5 data is global in extent, like COSMIC-1.

The vertical gridded resolution of COSMIC-1/KOMPSAT-5 wetPrf soundings is 0.1 km from an elevation of 0.1 km to 39.9 km. Meanwhile, COSMIC-2 sounding measurements have a 0.05 km resolution from the lowest valid level to near the tropopause. Then it has a 0.1 km gridded resolution that continues upward to 59.9 km. Each GNSS RO sounding measurement quantifies horizontally-integrated atmospheric temperature and water vapor over a few 100 km along a GNSS transmitter signal ray path centered at the tangent point.

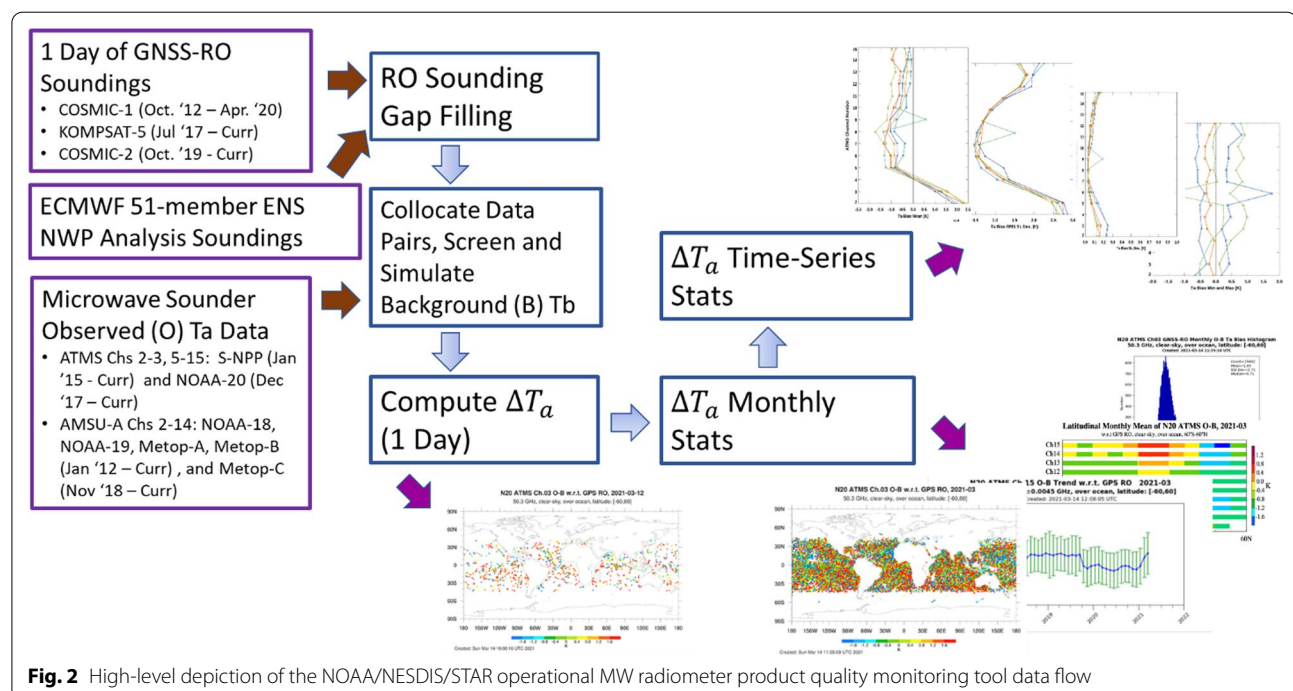
The global mean difference between COSMIC-1 sounding temperature and UK Met Office (UKMO) assimilated data observations, and National Centers for Environmental Prediction (NCEP) and Japan Meteorological Agency (JMA) reanalysis from 8 to 30 km is estimated to be about 0.65 ± 0.02 K (Kishore et al. 2008). A more recent study of soundings over the Arctic estimated a structural uncertainty (due to different data processing approaches) of about 0.72 K (Yu et al. 2018). The precision of COSMIC-1 GNSS RO soundings, estimated by comparison of closely collocated Challenging Minisatellite Payload (CHAMP) and Scientific Application Satellite-C (SAC-C) GNSS RO soundings, is approximately 0.05 K in the upper troposphere and lower stratosphere (Anthes et al. 2008). In lower tropospheric regions with significant water vapor—e.g., where the temperature is higher than 270 K—the precision reduces to about 0.1 K. These findings reveal a much closer agreement between GNSS RO soundings from different programs than comparisons with soundings from data assimilation and reanalysis. This is expected because the measurement technology and processing technique are very similar between GNSS RO programs. Meanwhile, the data assimilation and reanalysis are created from many data resources with disparate measurement technologies—e.g., microwave and infrared sounders and radiosondes—that have unique uncertainties. Finally, the accuracy of COSMIC-2 measurements between the six microsattellites has been assessed recently by Ho et al. (2020).

3 Methodology

A high-level depiction of the NOAA/NESDIS/STAR operational MW radiometer product quality monitoring tool data flow can be found in Fig. 2. This figure shows that a single day of COSMIC and KOMPSAT-5 GNSS RO atmospheric temperature and moisture soundings, imported from the CDAAC and NOAA/NESDIS/STAR data sources mentioned earlier, are first gap-filled with ECMWF 51-member ENS NWP analysis sounding outputs. This gap-filling occurs at elevations between the earth's surface and the lowest valid RO retrieved temperature and moisture values. It is also applied above the highest elevation containing valid RO retrieved values until the top boundary of the ECMWF sounding is reached. This gap-filling is performed to create soundings stretching from the surface to an elevation of about 80 km that can be readily imported into the CRTM. After inputting the operational MW sounder data from AMSU-A Chs 2–14 and ATMS Chs 2–3 and Chs 5–15 into the analysis, collocation between the gap-filled soundings and the satellite data is carried out. For identified matched pairs, the sounding quality is further scrutinized, and outlier soundings are screened out. The remaining matched-pair atmospheric soundings are then imported into the CRTM to generate simulated ATMS or AMSU-A Tb values. The simulated Tb values based on the blended soundings can be used as a reference standard that the AMSU-A and ATMS operational Ta or Tb products can be compared to.

Computing ΔT_a for the RO sounding and MW radiometer matched pairs identified within a given day largely removes the meteorological signal from the MW radiometer data. The ΔT_a consists mainly of the instrument, sounding, and CRTM simulation errors. It also includes errors related to the different spatial characteristics of the measurements and the spatial/temporal displacement between “collocated” measurements. The ΔT_a from a given day are first used to generate daily bias maps. Using 30-day retrospective ΔT_a , monthly maps, and plots from monthly statistical analysis—e.g., histograms and global and latitudinal mean and standard deviation—can be created. These daily- and monthly-scale outputs can be found with about 2-day latency on the STAR ICVS for each NOAA operational MW radiometer. Finally, longer time series statistics can be computed and plotted, but such outputs are reserved for more in-depth studies of bias behavior. This method has been implemented for several years within STAR. Iacovazzi et al. (2020) described the architecture and analysis process associated with the first build of this critical software tool. Since the tool screening methods have undergone appreciable change since that article, an overview of the screening techniques is described in the following.

In this analysis, physics-based screening methods are applied, and the remainder of the data enter the statistical computations without any process for outlier rejection. This is done to preserve the natural variability of the ΔT_a data, and to ensure that the relatively



small pre-COSMIC-2 monthly sample sizes are as large as possible. The primary screening methods described below focus on limiting space and time differences between MW and GNSS RO data, eliminating scenes with highly variable surface emissivity and clouds, restricting elevation-dependent location variations in the GNSS RO soundings, and ensuring adequate sounding coverage in the vertical to represent a given ATMS or AMSU-A channel weighting function.

The time and space difference collocation criteria between a given blended GNSS RO/ECMWF sounding and the MW radiometer data are no more than three hours and less than 50 km, respectively. If multiple MW radiometer pixel measurements satisfy these collocation criteria, the one closest to the related blended GNSS RO/ECMWF sounding is chosen, and the others are discarded. Note that the spatial distance collocation criterion of a given sounding is tested at the weighting function peak altitude for each MW radiometer FOV. For reference, ATMS and AMSU/MHS nadir-view weighting function peak elevations are provided in Table 1. It is also important to note that the weighting function peak elevation is a function of the radiometer scan position and channel. This is accounted for during data processing through look-up tables that associate microwave channel, scan angle, and weighting function peak elevation. The scan angle is retained as an input into the CRTM so T_b can be simulated using the actual radiometer view.

The collocated gap-filled GNSS RO/ECMWF soundings and MW radiometer measurements must be quality screened before the CRTM simulations and subsequent comparisons with observations can be performed. There are several screening criteria applied. Data are limited to those samples falling equatorward of 60° latitude. Microwave radiometer channels influenced by the surface—i.e., ATMS Chs 2–3 and 5–6 and AMSU-A Chs 2–5 that have frequencies less than 54.4 GHz—are limited to the ocean only and screened for clouds using a method similar to Weng et al. (2003). Relatively large MW surface emissivity spatial variability, and difficulties screening out regions with non-precipitating clouds, are the reasons that RO data over all land surfaces are screened out for these MW sounder channels. Large surface emissivity variability causes RO and MW data to have increased measurement differences during the collocation process. It also makes simulating MW surface channels with the CRTM extremely difficult. Meanwhile, ATMS Chs 7–15 and AMSU-A Chs 6–14 between 54.4 GHz and 57.29 GHz—negligibly influenced by surface emission because of their relatively high peak weighting functions—are screened out only for regions with a topographic elevation higher than 2 km. Overland soundings that contain clouds with

appreciable precipitation are identified and rejected using a method by Grody et al. (2001).

As mentioned previously, the GNSS radio signal passes through the atmosphere, and its ray path is bent over due to variations of atmospheric refraction. As the GNSS transmitters and GNSS RO receivers move, so does the perigee point's earth location (also called the tangent point), which causes a single GNSS RO profile to vary its geographic location with altitude. In this analysis, soundings are rejected with greater than 360 km maximum sounding measurement earth location variation with altitude. This threshold is chosen because the GNSS RO horizontal resolution is about 300 km. This constraint leads to about 5% or less of soundings being removed from the analysis. When the sounding geolocation variability with altitude is constrained, it also allows spatial constraints to be placed on the collocation process, making it much more efficient.

The final sounding screening criteria ensure they have adequate depth to produce meaningful radiative transfer model simulations. For MW sounder channels where less than 5% of the surface radiation is transmitted to the sensor, blended GNSS RO/ECMWF sounding data must penetrate at least to an elevation where only 5% of the emission reaches the satellite. For channels with more than 5% of the surface radiation transmitted to the radiometer, the maximum sounding pressure level with valid data must be greater than 1000 hPa if the elevation is sea level or below. For heights greater than sea level, soundings are screened to make sure they penetrate within 1.0 km of the surface.

As described earlier in this section, once the data have been appropriately collocated and screened, the gap-filled GNSS RO/ECMWF soundings can be input into the CRTM to generate the simulated MW radiometer T_b values. This allows the simple difference between the NOAA operational MW radiometer observed T_a and the CRTM-simulated background T_b values to be computed. This paper's long-term time series and statistical results are based on ΔT_a values from all individual collocated radiometer and gap-filled GNSS RO/ECMWF sounding data accumulated over specified periods. In this study, two distinct periods are analyzed. The first period (TP1), stretching from May 1, 2017, to September 30, 2019, denotes post-Block-2 ATMS algorithm update data processing and exclusive use of COSMIC-1/KOMP-SAT-5 soundings. The second period (TP2), extending from October 1, 2019, to December 31, 2020, marks the expansion of the analysis to include COSMIC-1, KOMP-SAT-5, and COSMIC-2 soundings. Note that the last day of COSMIC-1 data availability from CDAAC is April 25, 2020. This strategy of performing separate TP1 and TP2 analyses is designed to highlight the differences between

results achieved when the COSMIC-2 soundings are added.

4 COSMIC-2 impacts on the RO-based NOAA microwave satellite data quality monitoring system

Statistics in this section are classified by parameter and statistics type, MW instrument and channel, geographic region of interest, and time duration. The goal is to compare and contrast NOAA/NESDIS/STAR RO-based MW product quality monitoring output before and after COSMIC-2 soundings were added to the analysis on October 1, 2019. Thus, results are shown to emphasize pre- and post-COSMIC-2 integration behavior for each classification. The results are organized to present the parameters from simple to complex, the time duration from longest to shortest, and the region of interest from largest to smallest. For some analyses, redundant results for similar MW instrument channels are not shown since that would increase the complexity of the discussion without conveying new information.

The underlying analysis statistical parameters in this section are monthly GNSS RO and MW instrument matched data sample count (C); O-B T_a bias monthly mean ($\mu(\Delta T_a)$) and standard deviation ($\sigma(\Delta T_a)$) values; and inter-sensor monthly mean T_a bias ($\mu(\delta T_a)$) values based on $\mu(\Delta T_a)$ “double-difference” computations between sensors. The regions of interest are the globe (60°S to 60°N) and the 12 10° latitude bands between 60°S to 60°N, and the time durations are monthly, TP1 and TP2. The MW instruments and channels used in the analysis are N18, N19, MEA, MEB, and MEC AMSU-A Chs 2–14, and S-NPP and N20 ATMS Chs 2–3 and Chs 5–15. Some of the analysis showcases separate results for radiometer channels influenced by surface radiation (ATMS Chs 2–3 and 5–6 and AMSU-A Chs 2–5) from those not influenced by surface radiation (ATMS Chs 7–15 and AMSU-A Chs 6–14).

The results are presented in the following four subsections. Global and latitudinal GNSS RO and MW instrument matched data sample population changes from TP1 to TP2 are shown in Sect. 4.1. The Global TP1 and TP2 mean and standard deviation of $\mu(\Delta T_a)$ and the time-period differences are provided and discussed in Sect. 4.2. Statistics related to $\mu(\Delta T_a)$ and $\sigma(\Delta T_a)$ time series, computed for the global region of interest, are provided in Sect. 4.3. Differences of TP1 and TP2 mean and standard deviation of $\mu(\Delta T_a)$ time series, analyzed over the 12 latitude bands, are also presented in this subsection to elicit a greater understanding of time series behavior. Finally, in Sect. 4.4, statistical analysis of $\mu(\delta T_a)$ double-difference values are presented.

4.1 Global and latitudinal GNSS RO and MW sounder matchup data sample population statistics

Before COSMIC-2 data became available in October 2019, the daily number of atmospheric temperature and moisture soundings available from COSMIC-1 was about 100–300, and from KOMPSAT-5 was about 215–250. After COSMIC-2 data started to flow, the COSMIC-1 data rate slowed to less than 70 soundings per day until it stopped completely from CDAAC on April 25, 2020. The KOMPSAT-5 data flow has dropped from October 2019 to a rate of about 140–200 soundings per day. Meanwhile, the number of COSMIC-2 soundings could range from about 3000 to 5000 per day. Thus, COSMIC-2 has increased the monthly number of GNSS RO soundings available to match with the MW radiometer data from the order of 10^4 to about 10^5 . The data analysis screening and collocation processes presented in Sect. 3 reduce the number of GNSS RO soundings available for comparison with MW radiometer data by more than 85% for channels predominantly influenced by surface radiation and 50% for channels that are not.

Maps of global monthly-accumulated ΔT_a for N20 ATMS Ch 2 and Ch 10 are provided in Fig. 3A, B, respectively. In these figures, each point represents the location of a COSMIC-1/KOMPSAT-5 GNSS RO sounding and collocated N20 observation that was acquired during September 2019, which is the last month of TP1. These two channels are chosen to represent the salient characteristics of channels that are primarily subject to surface radiation (e.g., ATMS Ch 2) and those that are not (e.g., ATMS Ch 10). The results from all surface-influenced channels are consistent with each other, as are those from the sounding channels. Thus, there is no need to show results for all of the channels since channels with similar physical characteristics show similar results.

These figures clearly demonstrate that upper-air sounding channels such as ATMS Ch 10 have more points than surface-influenced channels like ATMS Ch 2. This is due to the omission of data matchups over land, and greater prevalence of clouds and precipitation screening, for surface-influenced channels. The color shade of each point represents a ΔT_a range to quantify its value crudely. The data sparseness in these figures—227 points for Ch 2 and 765 points for Ch 10—reveal the waning COSMIC-1/KOMPSAT-5 GNSS RO sounding populations by the end of TP1. The monthly ΔT_a maps for N20 ATMS Ch 2 and Ch 10 for October 2019 are provided respectively in Fig. 3C, D, so the reader can appreciate that a large number of observations are brought to bear in the analysis with the addition of COSMIC-2 during TP2.

For Fig. 3A, C, the spatial and temporal difference between the ATMS and GNSS RO data—i.e., up to 50 km and 3 h—can create a relatively large dispersion in the

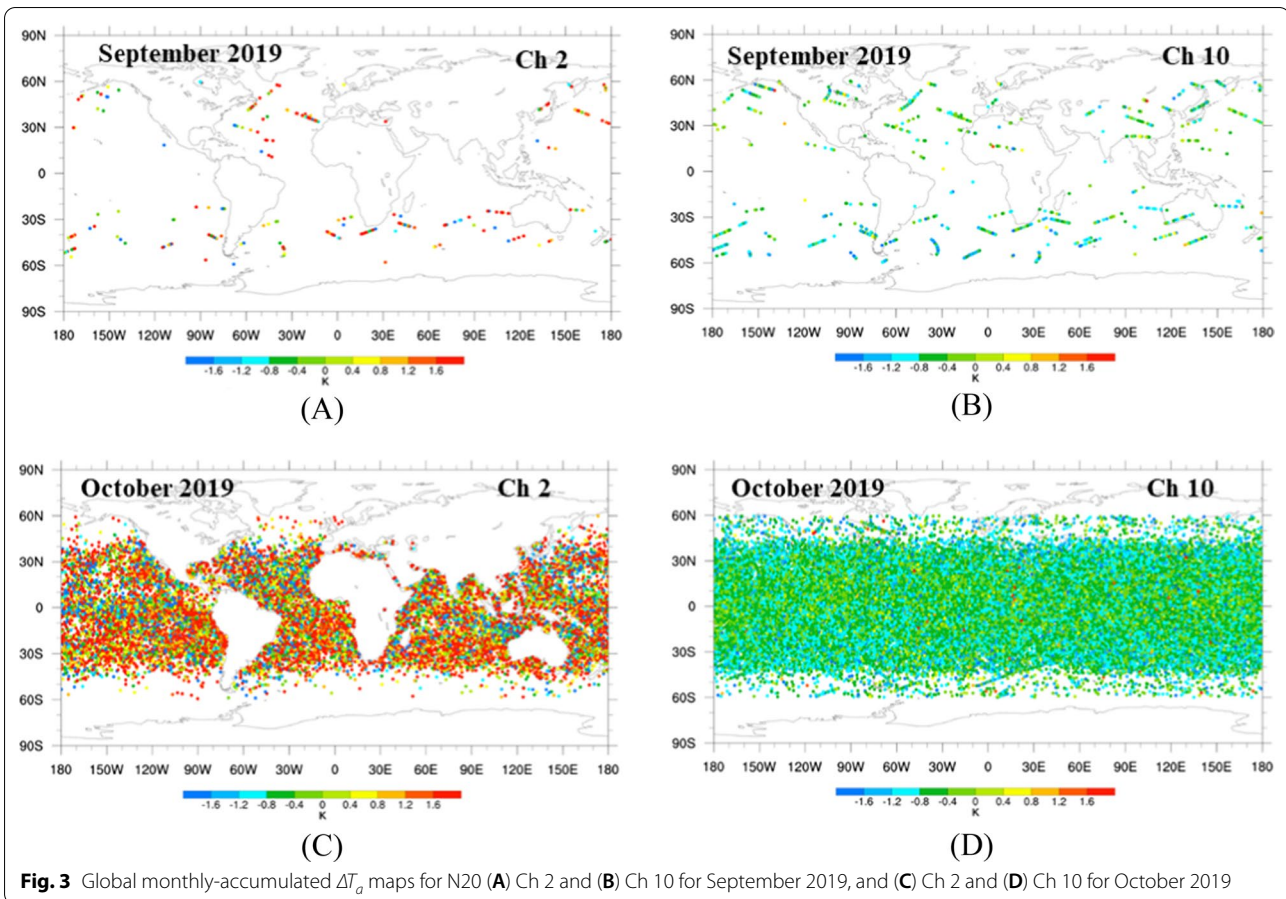


Fig. 3 Global monthly-accumulated ΔT_a maps for N20 (A) Ch 2 and (B) Ch 10 for September 2019, and (C) Ch 2 and (D) Ch 10 for October 2019

ΔT_a values. This dispersion can be related to surface emissivity variation due to broken sea ice, inhomogeneous cloud cover, regional clear-sky wind-induced sea surface foam, coastlines, etc. So, a big ΔT_a value spread for Channel 2 is expected. For ATMS Ch 10 in Fig. 3B, D, the relatively homogenous nature of these upper-tropospheric and lower-stratospheric scenes is clearly reflected in the data.

It becomes clear from these figures that COSMIC-1/KOMPSAT-5 are concentrated in the subtropics and mid-latitudes, while the COSMIC-2 data primarily populate the tropics and subtropics. The latitudinal distribution of TP2-mean minus TP1-mean GNSS-RO and MW sounder monthly matched sample numbers shown in Fig. 4A reveals this in more detail for N20 and NPP ATMS Ch 2 and N18, N19, MEA, MEB, and MEC AMSU-A Ch 2. A similar plot for ATMS(AMSU-A) Ch 10(9) is shown in Fig. 4B for all satellites.

Figure 4A, B show COSMIC-2 data augmentation peaks at about 2500 and 7000 samples per month, respectively. This data augmentation from COSMIC-2 is not distributed uniformly. It maximizes near the

equator and falls to less than 300 samples per month between 40° to 50° . Poleward of 50° , there is actually average decreases in monthly sample number from TP1 to TP2. This reveals the attrition of COSMIC-1/KOMPSAT-5 data between the two time periods because COSMIC-2 data do not extend to these latitude bands. An interesting feature in Fig. 4B is that stark difference between ATMS and AMSU-A maxima, which shrinks considerably in Fig. 4A. This can be explained by the increased data screening for surface-influenced channels compared to those that are not surface-influenced.

The strong latitudinal dependence of TP2-mean minus TP1-mean GNSS-RO and MW sounder data monthly matched samples will alter the weight of each latitude band to global mean and standard deviation statistics. Figure 5A, B illustrate this concept by giving the mid-latitude to tropics ratio (R) of monthly sample counts averaged over TP1 ($\mu[C]^{TP1}$) and TP2 ($\mu[C]^{TP2}$), respectively, for the MW sounder channels and instruments included in this study. The value R is computed using the following equation

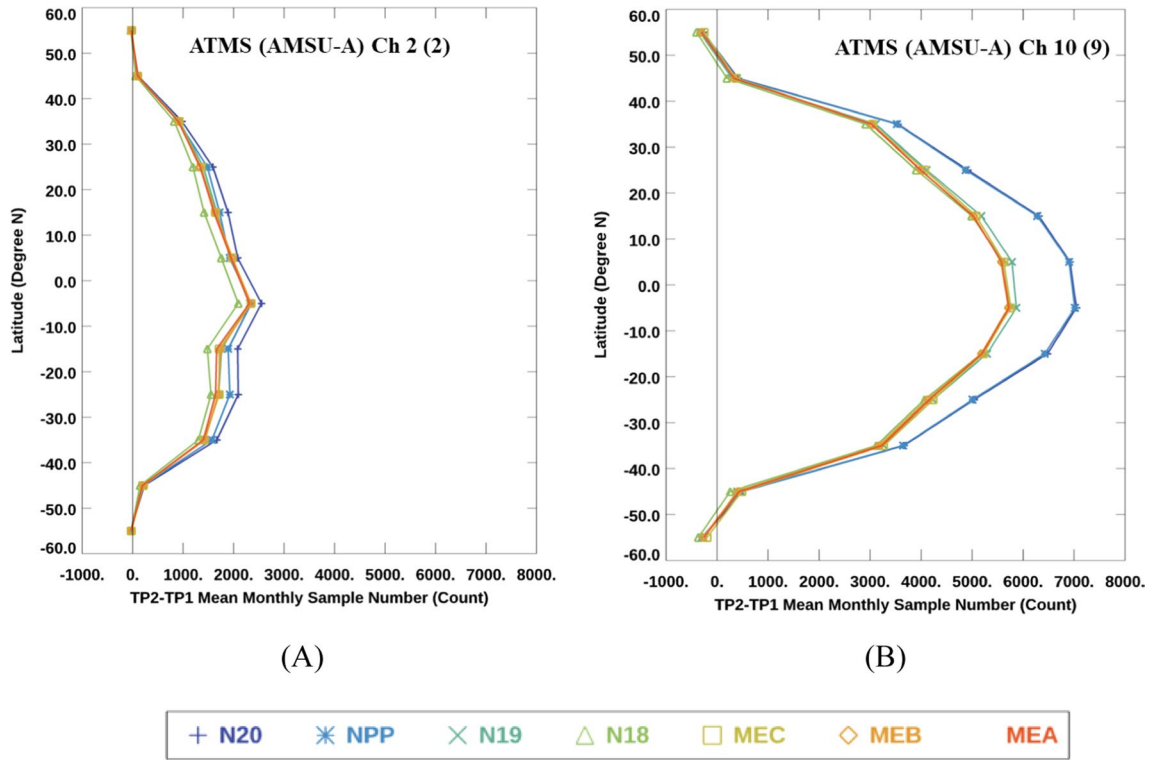


Fig. 4 The TP2-mean minus TP1-mean latitudinal distribution of GNSS-RO and MW sounder monthly matched samples for (A) N20 and NPP ATMS and N18, N19, MEA, MEB, and MEC AMSU-A Ch 2, and (B) N20 and NPP ATMS Ch 10 and N18, N19, MEA, MEB, and MEC AMSU-A Ch 9

$$R_{TPX} = 100.0 \times \frac{\mu[C_{40^{\circ}N:60^{\circ}N}]^{TPX} + \mu[C_{60^{\circ}S:40^{\circ}S}]^{TPX}}{\mu[C_{20^{\circ}S:20^{\circ}N}]^{TPX}},$$

where TPX is either TP1 or TP2. Figure 5A shows that in TP1 there are on average 100% to 350% more samples in the mid-latitudes compare to the tropics, with the highest values observed in channels larger than ATMS(AMSU-A) Ch 9(8). This would skew statistics according to ΔT_a values in the mid-latitudes. Figure 5B shows that in TP2 the mid-latitudes have only 10% of the average monthly sample numbers found in the tropics. This reflects a major shift in this period for instrument ΔT_a statistics to be skewed towards data in lower latitudes. This finding is important to note as the remaining results are presented.

It is clear now that COSMIC-2 (COSMIC-1/KOMP-SAT-5) data extend from 45°S to 45°N (60°S and 60°N). At this point, it is important to justify the motivation to perform this analysis between 60°S and 60°N, even though there is a disparity in latitudinal data extent between the GNSS RO missions. Applying the 45° limit to COSMIC-1/KOMP-SAT-5 data would have a sizable effect on TP1 results, since only about 30% to 45% of its data resides equatorward of 45° by the end of TP1. Removing this data would not accurately reflect MW sounder data monitoring system behavior before the COSMIC-2 data

were introduced to the system in TP2. It is the goal of the paper to understand the impact of the COSMIC-2 data on the existing MW sounder data monitoring system.

4.2 TP1 and TP2 global $\mu(\Delta T_a)$ statistics

To capture the salient character of ΔT_a at the coarsest space and time scales, $\mu(\Delta T_a)$ values computed over the 60°S to 60°N global (gl) region, $\mu(\Delta T_a)_{gl}$, are averaged separately over the TP1 and TP2 time periods—i.e., $\mu[\mu(\Delta T_a)_{gl}]^{TP1}$ and $\mu[\mu(\Delta T_a)_{gl}]^{TP2}$. The difference of these quantities, $\mu[\mu(\Delta T_a)_{gl}]^{TP2-TP1}$, can reveal overall bias shifts of the MW sounding data quality monitoring results after COSMIC-2 data are introduced into the data stream. In Fig. 6A, B, $\mu[\mu(\Delta T_a)_{gl}]^{TP1}$ and $\mu[\mu(\Delta T_a)_{gl}]^{TP2}$ are shown for N18, N19, MEA, MEB, and MEC AMSU-A Chs 2–14 and NPP and N20 ATMS Chs 2, 3, and 5–15. Both figures show that these values are between 1.0 K and 2.5 K for ATMS and AMSU-A Ch 2 and Ch 3, and between -2.0 K and 0 K for all other channels except N19 AMSU-A Ch 8. The differences between the two time periods seem relatively small, but the nature of even subtle differences need closer scrutiny.

To elucidate the change of $\mu[\mu(\Delta T_a)_{gl}]^{TP1}$ in TP2, $\mu[\mu(\Delta T_a)_{gl}]^{TP2-TP1}$ values are plotted in Fig. 6C. The values in Fig. 6C are between 0.3 K and 0.5 K for ATMS

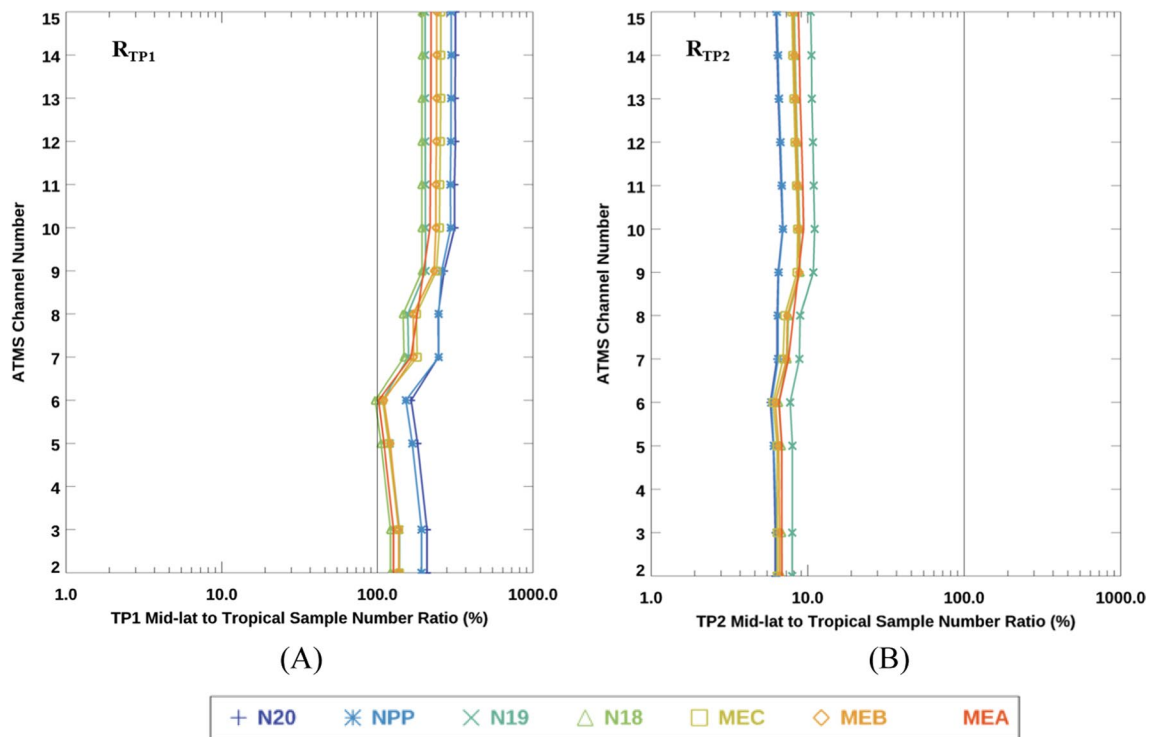


Fig. 5 The (A) R_{TP1} and (B) R_{TP2} values for N18, N19, MEA, MEB, and MEC AMSU-A, and NPP and N20 ATMS are plotted for each ATMS channel. Except for ATMS Ch 2 and Ch 3, the corresponding AMSU-A channel is the ATMS channel number minus one. The vertical line in each plot constitutes the 100% value

Chs 2–3, and between 0 K and 0.2 K for the corresponding AMSU-A channels. The relatively large and consistent ATMS difference values may be due to the non-zero instrument reflector emissivity algorithm correction (Yang et al. 2016) implemented in ATMS data processing in October 2019 coupled with the similar reflector emissivity values in these channels for N20 and NPP ATMS units (Yang, personal communication). The AMSU-A data processing algorithm does not apply any instrument reflector emissivity correction.

For ATMS(AMSU-A) Chs 5–9(4–8), Fig. 6C shows the $\mu[\mu(\Delta T_a)_{gl}]^{TP2-TP1}$ values have a downward trend from 0.1 K to -0.2 K. Possible reasons for this behavior will be explored in the Sect. 4.3. The values for most instruments are within about 0.1 K of each other, except for a prominent N19 AMSU-A Ch 8 positive anomaly that is evident in both figures. This anomaly appeared shortly after the launch of N19 and is associated with a noise equivalent delta temperature (NEDT) anomaly that varies between 0.6 K and 1.2 K. The NEDT specification for this AMSU-A channel is 0.25 K. This NEDT change is also associated with anomalous gain changes that lead to significant N19 AMSU-A Ch 8 $\mu(\Delta T_a)_{gl}$ time-series variability. This anomaly is discussed in more detail in a paper by Iacovazzi et al. (2020). Note that MEA Ch 7 and Ch 8

have no values because there is not data for these channels. The $\mu[\mu(\Delta T_a)_{gl}]^{TP2-TP1}$ values in Fig. 6C reveal decreases from 0.0 K to -0.5 K from ATMS(AMSU-A) Chs 10–15(9–14), and values for most instruments for a given channel can vary from each other by 0.1 K to 0.7 K. The nature of the relatively large decrease will also be discussed further in Sect. 4.3.

Similar analyses for TP1 and TP2 standard deviation of $\mu(\Delta T_a)_{gl}$ —i.e., $\sigma[\mu(\Delta T_a)_{gl}]^{TP1}$ and $\sigma[\mu(\Delta T_a)_{gl}]^{TP2}$ —are shown in Fig. 7A, B, respectively. Meanwhile, their difference, $\sigma[\mu(\Delta T_a)_{gl}]^{TP2-TP1}$, is given in Fig. 7C. Figure 7A shows that $\sigma[\mu(\Delta T_a)_{gl}]^{TP1}$ values for ATMS(AMSU-A) Chs 5–11 (4–10) to be between about 0.025 K to 1.0 K. For ATMS and AMSU-A Ch 2 and Ch 3, these values range between 0.125 K to 0.225 K, while for ATMS(AMSU-A) Chs 12–15 (11–14), they have values that increase from 0.075 K to about 0.15 K. Clear differences can be found in 7.B for $\sigma[\mu(\Delta T_a)_{gl}]^{TP2}$. In this figure, the variability between satellite instruments is much smaller. In addition, the ATMS(AMSU-A) Chs 12–15(11–14) values in Fig. 7B increase from 0.1 K to about 0.5 K. This is a relatively large increase from the values in Fig. 7A.

The TP2–TP1 differences for these statistics, $\sigma[\mu(\Delta T_a)_{gl}]^{TP2-TP1}$, shown in Fig. 7C are reduced by

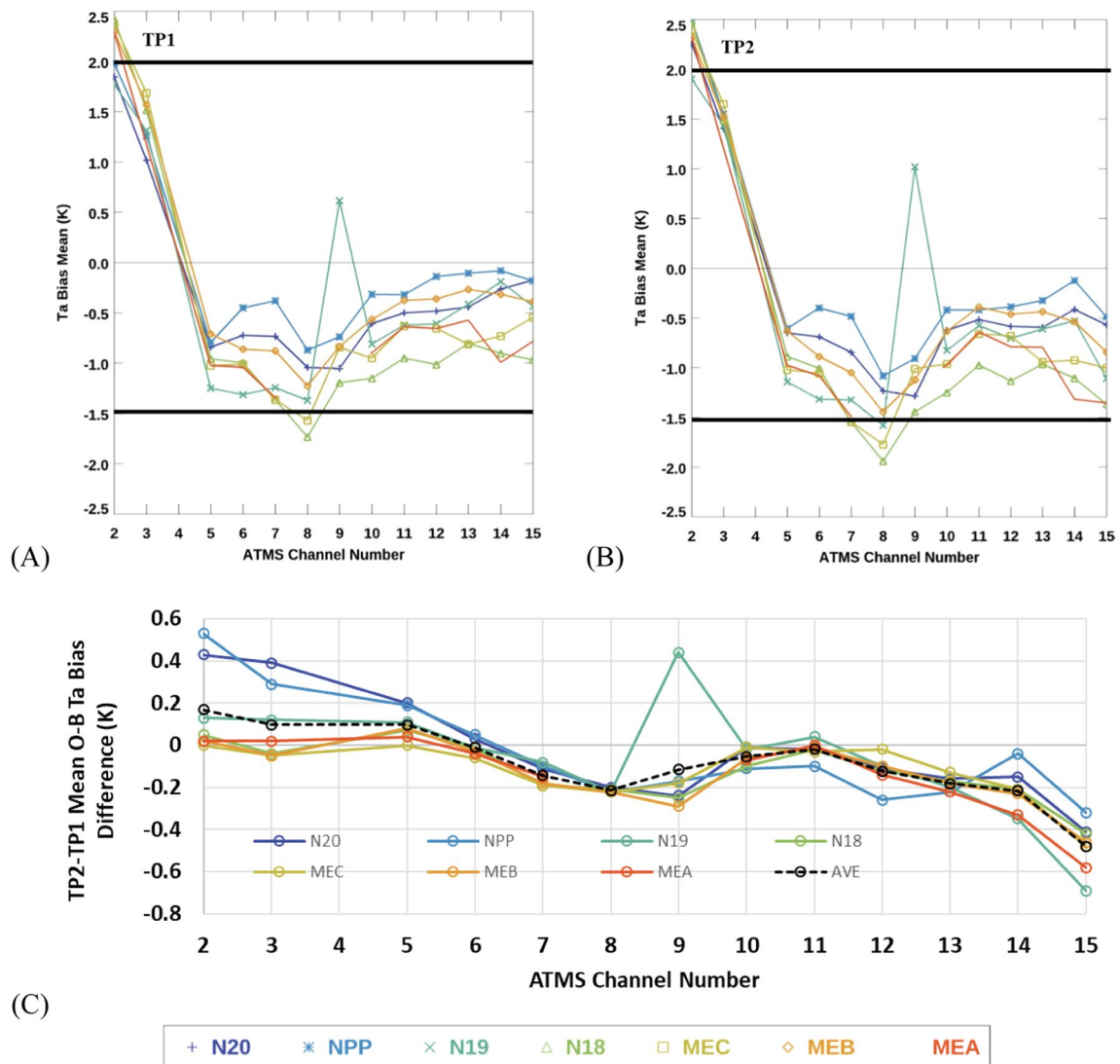


Fig. 6 (A) $\mu[\mu(\Delta T_a)_{gl}]^{TP1}$, (B) $\mu[\mu(\Delta T_a)_{gl}]^{TP2}$ and (C) $\mu[\mu(\Delta T_a)_{gl}]^{TP2-TP1}$ values for N18, N19, MEA, MEB, and MEC AMSU-A Chs 2–14, and NPP and N20 ATMS Chs 2–3 and 5–15, plotted for each ATMS channel. Except for ATMS Ch 2 and Ch 3, the corresponding AMSU-A channel is the ATMS channel number minus one. The thick black horizontal lines in **A** and **B** represents the region where most of the data fall for TP1

about -0.1 K for ATMS(AMSU-A) Chs 2–3 and 5(2–4), are near zero for ATMS(AMSU-A) Chs 6–11(5–10), and are increased from about 0.05 K to about 0.4 K for ATMS(AMSU-A) Chs 12–15(11–14). This significant increase in $\sigma[\mu(\Delta T_a)_{gl}]^{TP2-TP1}$ for these channels will be further investigated in Sect. 4.3.

4.3 TP1 and TP2 global $\mu(\Delta T_a)$ and $\sigma(\Delta T_a)$ statistics and TP2–TP1 latitudinal $\mu(\Delta T_a)$ statistics

The COSMIC-2 impacts to the NOAA operational MW radiometer data quality monitoring tool can be further highlighted and characterized by comparing and contrasting TP1 and TP2 $\mu(\Delta T_a)$ and $\sigma(\Delta T_a)$ statistics.

For this purpose, $\mu(\Delta T_a)_{gl}$ time series examples over these two time periods are presented first. The TP1-mean and TP2-mean and standard deviation of $\mu(\Delta T_a)$ time series analyzed in 10° latitude bins over the 60°S to 60°N global region of interest—i.e., $\mu[\mu(\Delta T_a)_{lat}]^{TP1}$, $\mu[\mu(\Delta T_a)_{lat}]^{TP2}$, $\sigma[\mu(\Delta T_a)_{lat}]^{TP1}$ and $\sigma[\mu(\Delta T_a)_{lat}]^{TP2}$ —is subsequently presented to provide a deeper understanding of time series behavior. The global monthly standard deviation O-B Ta bias, $\sigma(\Delta T_a)_{gl}$, time series (not shown) is used to calculate its root-mean-square (RMS) separately over TP1 and TP2. This provides a measure of uncertainty for $\mu(\Delta T_a)_{gl}$ values in this analysis.

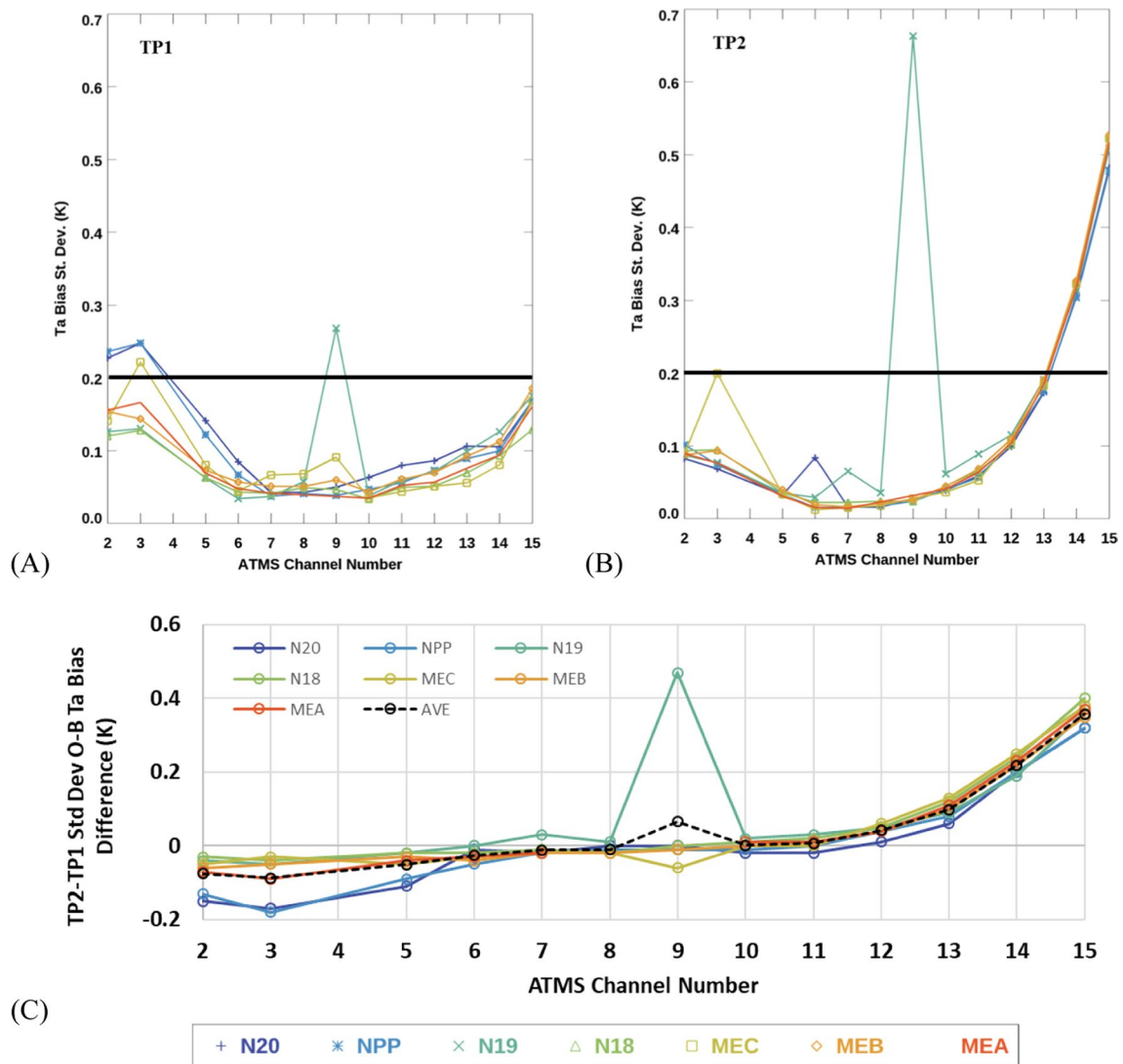


Fig. 7 (A) $\sigma[\mu(\Delta T_a)_{gl}]^{TP1}$, (B) $\sigma[\mu(\Delta T_a)_{gl}]^{TP2}$ and (C) $\sigma[\mu(\Delta T_a)_{gl}]^{TP2-TP1}$ values for N18, N19, MEA, MEB, and MEC AMSU-A Chs 2–14, and NPP and N20 ATMS Chs 2–3 and 5–15, plotted for each ATMS channel. Except for ATMS Ch 2 and Ch 3, the corresponding AMSU-A channel is the ATMS channel number minus one. The region below the thick black horizontal line in **A** and **B** represents where most of the data fall for TP1

In Fig. 8A, the $\mu(\Delta T_a)_{gl}$ time series during TP1 and TP2 are shown for ATMS and AMSU-A Ch 2 for all instruments. A vertical black line in this figure separates TP1 and TP2 in October 2019. This figure illustrates that AMSU-A and ATMS $\mu(\Delta T_a)_{gl}$ time series are generally more comparable with each other and become more stable from TP1 to TP2 for surface-influenced channels. One prominent feature of Fig. 8A is the large $\mu(\Delta T_a)_{gl}$ adjustments that occurred between September and October 2019. This may be a manifestation of the augmented quantity and latitudinal distribution shift of matched GNSS RO and MW matched samples after COSMIC-2 soundings are integrated, as shown in Figs. 4A and 5B.

The COSMIC-1/KOMPSAT-5 soundings populations shown in Fig. 3A near the end of TP1 cover from 60°S to 60°N, but are almost non-existent near the equator. This skewed latitudinal data distribution is reflected clearly in the R_{TP1} values presented in Fig. 5A. Data coverage limited to higher latitudes can relate to increased ΔT_a uncertainty associated with larger spatial variations of ocean temperature and surface emissivity. The surface emissivity variations in the mid-latitudes are related to greater instances of significant regional clear-sky wind-driven sea foam and the existence of sea ice. Less column-integrated water vapor exists on average in the mid-latitudes than in the tropics, which may manifest as latitudinal changes

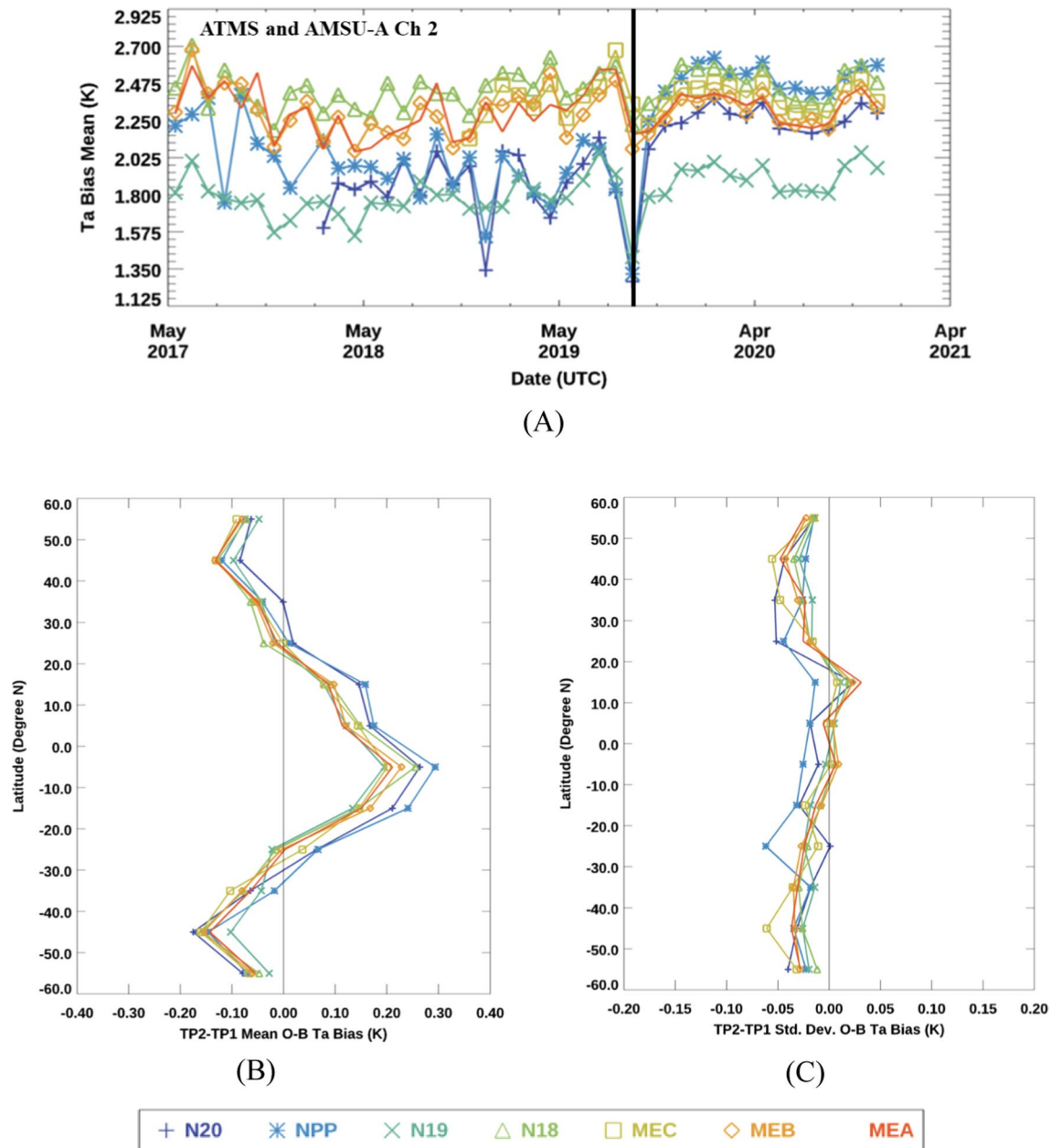


Fig. 8 (A) $\mu(\Delta T_a)_{gl}$ time series, (B) $\mu[\mu(\Delta T_a)_{lat}]^{TP2-TP1}$, and (C) $\sigma[\mu(\Delta T_a)_{lat}]^{TP2-TP1}$ for ATMS and AMSU-A Ch 2. The time series in the analysis include N18, N19, MEA, MEB, and MEC AMSU-A and NPP and N20 ATMS. The black line in **A** denotes October 2019, which separates TP1 and TP2

in RO-sounding uncertainties in the lower atmosphere between the two regions. Such variability can impact ΔT_a through latitude-dependent systematic and random biases in CRTM-simulated Tb values and/or earth-scene Ta spatial gradients. COSMIC-2, with its much larger number of samples and range limited to 45°S to 45°N, coupled with the latitudinal variations of ΔT_a related to the physical mechanisms described above, might explain

the large jump of data between $\mu(\Delta T_a)_{gl}$ values at the end of TP1 and the beginning of TP2 for ATMS and AMSU-A Ch 2. To reach a more definitive conclusion, this needs to be affirmed by in-depth analysis that is out of scope for this paper.

Further analysis has been performed to resolve latitude-dependent contributions to the TP1 to TP2 $\mu(\Delta T_a)_{gl}$ time-series changes shown in Fig. 8A. In

Fig. 8B, the TP2 minus TP1 (TP2–TP1) mean of $\mu(\Delta T_a)$ are computed for the 12 10° latitude bins from 60°S to 60°N, i.e., $\mu[\mu(\Delta T_a)_{lat}]^{TP2-TP1}$. This analysis accounts for changes in the latitude distribution of GNSS RO and MW data monthly matched samples between these two time periods, as given in the equation below:

$$\mu[\mu(\Delta T_a)_{lat}]^{TP2-TP1} = \frac{\mu[C_{lat}]^{TP2}}{\mu[C_{gl}]^{TP2}} * \mu[\mu(\Delta T_a)_{lat}]^{TP2} - \frac{\mu[C_{lat}]^{TP1}}{\mu[C_{gl}]^{TP1}} * \mu[\mu(\Delta T_a)_{lat}]^{TP1}.$$

In this equation, $\mu[\mu(\Delta T_a)_{lat}]^{TPX}$ is the time period average of $\mu(\Delta T_a)$ values for a given latitude band, and $\mu[C_{lat}]^{TPX}$ and $\mu[C_{gl}]^{TPX}$ are the time period average monthly data samples for a given latitude band and between 60°S to 60°N, respectively. Note that TPX can be TP1 or TP2. Figure 8B shows that $\mu[\mu(\Delta T_a)_{lat}]^{TP2-TP1}$ is between 0 K and 0.25 K (– 0.15 K and 0 K) equatorward (poleward) of 30° latitude. These changes sum to a net positive change of $\mu[\mu(\Delta T_a)_{lat}]^{TPX}$ from TP1 to TP2, which was shown in Fig. 6C.

Figure 8C is similar to Fig. 8B, except that the changes of $\sigma[\mu(\Delta T_a)_{lat}]^{TPX}$ values are given instead of $\mu[\mu(\Delta T_a)_{lat}]^{TPX}$. This figure indicates that COSMIC-2 soundings help reduce $\sigma(\Delta T_a)_{lat}$ time series for most latitude bands poleward of the tropics by about – 0.05 K. This integrates to greater overall stability for each instrument time series. This bolstered time series stability in TP2 supported by COSMIC-2 helps to resolve a 0.3 K difference seen in Fig. 8A between NPP and N20 ATMS Ch 2 after October 2019. This 0.3 K difference became apparent after the ATMS antenna emission correction was introduced into the ATMS operational algorithm. It is also found for most channels except ATMS Ch 15 (Yang et al. 2021).

The results for ATMS(AMSU-A) Ch 10(9) shown in Fig. 9A reveal less dramatic $\mu(\Delta T_a)_{gl}$ time-series changes compared to Fig. 8A for AMSU-A and ATMS Ch 2, although a slight $\mu(\Delta T_a)_{gl}$ value decrease and a clearer semi-annual time series signal become evident in TP2. This minor change is expected, as ΔT_a values are fairly uniform across globe, as seen in Fig. 3D. Figures 9B, C are analogous to Fig. 8B, C. Figure 9B shows that $\mu[\mu(\Delta T_a)_{lat}]^{TP2-TP1}$ is between – 0.1 K and 0 K (0 K and 0.1 K) equatorward (poleward) of 40° latitude, which integrates to a small net negative change of $\mu[\mu(\Delta T_a)_{gl}]^{TPX}$ from TP1 to TP2. Figure 9C, shows only very small (<0.02 K) changes of $\sigma[\mu(\Delta T_a)_{lat}]^{TP2-TP1}$ values over all latitudes. This adds up to very little change in $\sigma[\mu(\Delta T_a)_{gl}]^{TPX}$ between the time periods. On the other hand, the remaining variation in the time series seems to reveal a synchronized semi-annual bias in all ATMS and AMSU-A units in

TP2 that was not readily apparent in TP1. From the ATMS weighting function shown in Fig. 1, ATMS Ch 10 and AMSU-A Ch 9 are not affected significantly by the atmospheric layer below 8 km or above 35 km. This minimizes the possibility of any latitudinal variability due to latitude-dependent water vapor and surface

temperature and emissivity variance from below 8 km, and ionospheric impacts above 30 km.

Figure 6C in Sect. 4.2 showed that $\mu[\mu(\Delta T_a)_{gl}]^{TP2-TP1}$ values have a downward trend from 0.1 K to – 0.2 K for ATMS(AMSU-A) Chs 5–9(4–8). The downward trend exhibited for these channels may be linked to the results in Figs. 8B and 9B. Figures 8B and 9B shows examples of $\mu[\mu(\Delta T_a)_{lat}]^{TP2-TP1}$ for a window and a column water vapor influenced channel, respectively. Tropical and subtropical contributions to $\mu[\mu(\Delta T_a)_{gl}]^{TP2-TP1}$ values are positive for Fig. 8B, and negative for Fig. 9B. As ATMS(AMSU-A) Ch 5(4) increases to Ch 9(8), the MW weighting function shifts radiometric contributions from mainly the surface to the water–vapor-rich atmosphere layer below 8 km. This degree of surface and water vapor influence for a given channel may explain the downward trend from 0.1 K and – 0.2 K seen in Fig. 6C.

Figure 10A reveals a much different story for ATMS(AMSU-A) Ch 15(14). A clear overall –0.4 K bias shift and 0.75 K amplitude semi-annual cycle materialize in the $\mu(\Delta T_a)_{gl}$ time series in this figure after COSMIC-2 soundings were added to the analysis. Figure 10B shows the $\mu[\mu(\Delta T_a)_{lat}]^{TP2-TP1}$ is between – 0.25 K and 0 K (0 K and 0.05 K) equatorward (poleward) of 20° latitude, which integrates to the – 0.4 K net negative $\mu[\mu(\Delta T_a)_{gl}]^{TPX}$ change from TP1 to TP2. Figure 10C, shows quite large 0.08 K to 0.15 K changes of $\sigma[\mu(\Delta T_a)_{lat}]^{TP2-TP1}$ values between 20°S and 20°N. Two less prominent $\sigma[\mu(\Delta T_a)_{lat}]^{TP2-TP1}$ peaks are found between 30°N and 40°N and 30°S and 40°S. This latitudinal profile integrates to the relatively large change in the $\mu(\Delta T_a)_{globe}$ time-series standard deviation.

This bias variability pattern has two prominent possible causes. The first is the sizable shift in monthly matched GNSS RO and MW sample population towards the tropics and sub-tropics compared to the mid-latitudes, as shown in Fig. 5A, B. The second is that during TP1 and TP2 the COSMIC-1/KOMPSAT-5 GNSS RO soundings are gap-filled with ECMWF sounding data above 40 km, and during TP2 the COSMIC-2 soundings are gap-filled with these data only above 60 km. The COSMIC-2 soundings between 40 and 60 km are retrieved using a

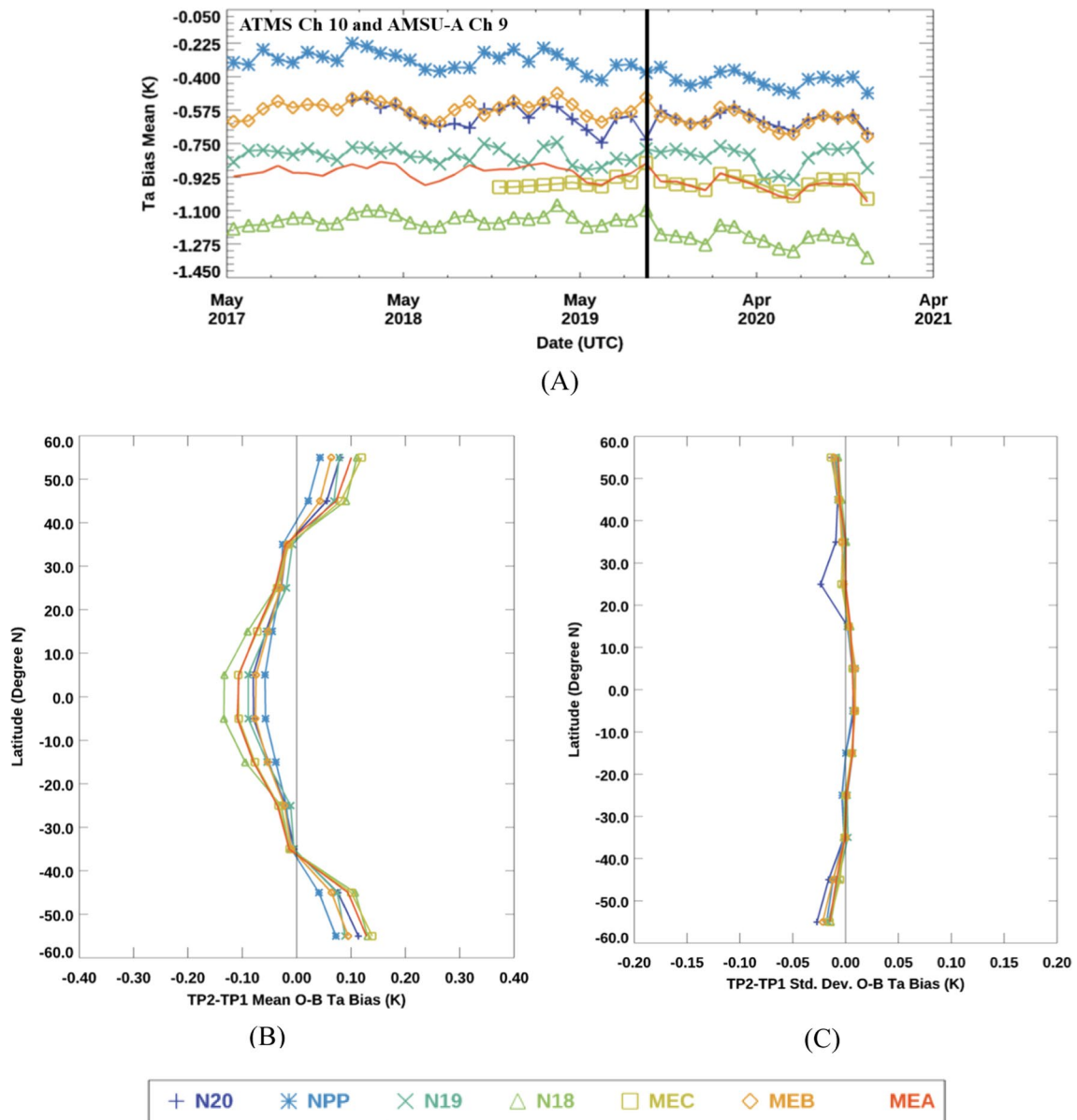


Fig. 9 (A) $\mu(\Delta T_a)_{gl}$ time series, (B) $\mu[\mu(\Delta T_a)_{lat}]^{TP2-TP1}$, and (C) $\sigma[\mu(\Delta T_a)_{lat}]^{TP2-TP1}$ for ATMS Ch 10 and AMSU-A Ch 9. The time series in the analysis include N18, N19, MEA, MEB, and MEC AMSU-A and NPP and N20 ATMS. The black line in **A** denotes October 2019, which separates TP1 and TP2

1D-Var algorithm that does not consider ionospheric effects on bending angle and refractivity.

These ionospheric effects can occur at regional to global spatial scales in the tropics and subtropics above 40 km, and at diurnal, seasonal, interannual, and interdecadal time scales. According to Lean et al. (2016), a semi-annual variation of total electron content is most pronounced between 25°S to 25°N. They also show an annual oscillation that exists between 40°S and 30°S.

These findings have been taken from a 17-year period between 1998 and 2015. This could affect $\mu(\Delta T_a)_{lat}$ mainly in the tropics between 20°S and 20°N, with another region of influence expected around 30°S to 40°S. The ECMWF soundings are partially conditioned by the ATMS and AMSU-A data input into the NWP model. This would cause CRTM Tb simulations based on the ECMWF sounding above 40 km to track much closer with the ATMS and AMSU-A observations, which

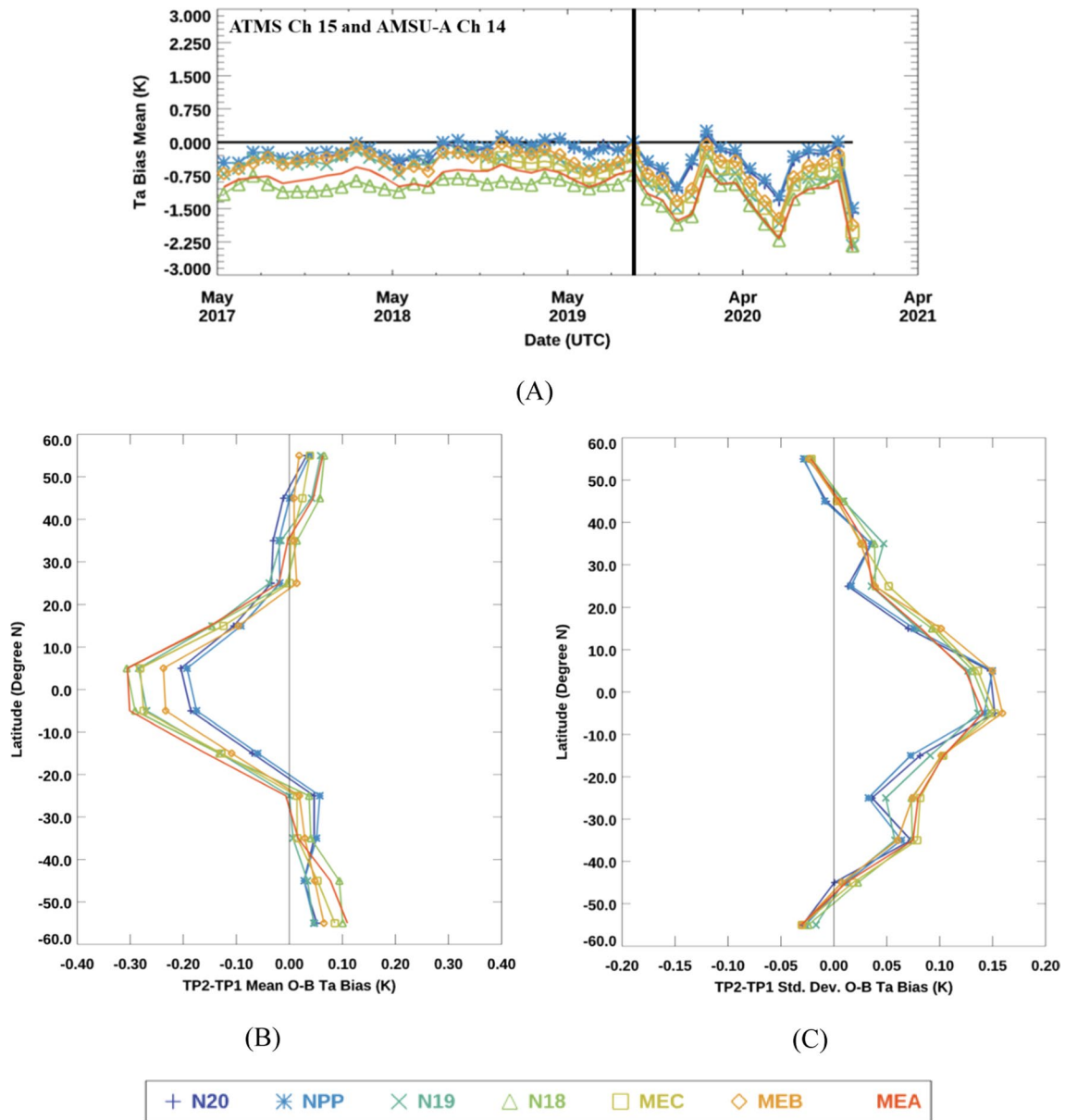


Fig. 10 (A) $\mu(\Delta T_a)_{gl}$ time series, (B) $\mu[\mu(\Delta T_a)_{lat}]^{TP2-TP1}$, and (C) $\sigma[\mu(\Delta T_a)_{lat}]^{TP2-TP1}$ for ATMS Ch 15 and AMSU-A Ch 14. The time series in the analysis include N18, N19, MEA, MEB, and MEC AMSU-A and NPP and N20 ATMS. The black line in **A** denotes October 2019, which separates TP1 and TP2

would greatly reduce any annual and semi-annual cycles in the $\mu(\Delta T_a)_{gl}$ time series. These issues with atmospheric sounding data between 40 and 60 km reveal limitations of tracking and trending ATMS(AMSU-A) Ch 15(14) Ta data. This may also apply to ATMS(AMSU-A) Ch 12–14(11–13) Ta data since their weighting functions shown in Fig. 1 have contributions from the layer between 40 and 60 km. Determining the degree to which a connection exists between GNSS RO soundings above

40 km and ionospheric variability need to be further explored in future work.

The $\mu[\mu(\Delta T_a)_{gl}]^{TP2-TP1}$ values in Fig. 6C reveal decreases from 0.0 K to -0.5 K from ATMS(AMSU-A) Chs 10–15(9–14), and values for most instruments for a given channel can vary from each other by 0.1 K to 0.7 K. The ATMS(AMSU-A) Chs 10–15 (9–14) spectral bands have weighting functions that span the stratosphere into the lower mesosphere. They do not have radiometric

contributions from the surface or water vapor rich lower atmosphere. This decreasing value with higher channel number may be due to the increasing MW weighting function peak altitudes coupled with the greater impact of the ionosphere on the COSMIC-2 sounding accuracy. An example of these possible ionospheric effects on $\mu(\Delta T_a)_{gl}$ is shown in Fig. 10A. Note that the behavior of the NPP result could be explained by the ATMS reflector emissivity correction, since NPP has a factor of 4–7 larger reflector emissivity compared to N20 for these channels.

The results found here and in Sect. 4.2 demonstrate that the latitudinal distribution of the GNSS RO sounding population before and after COSMIC-2 creates shifts in the RO-based $\mu(\Delta T_a)_{gl}$ values in the MW sounder product quality monitor. Together, the two subsections stress that to avoid these shifts, the RO data not only need to have a large enough population to deduce meaningful statistics, but their latitudinal population distribution needs to be relatively stable over time.

In Figs. 8A, 9A, and 10A, the global monthly standard deviation, $\sigma(\Delta T_a)_{gl}$, associated with each $\mu(\Delta T_a)_{gl}$ value in the time series is not shown to prevent overcrowding of plot information. It is important though to know

how the $\sigma(\Delta T_a)_{gl}$ values vary from TP1 to TP2. With a population of standard deviation values, it is important to convert each standard deviation to a variance, find the mean of the variances, and then convert this mean variance back to standard deviation. Since variance is the standard deviation squared, then this process amounts to a RMS operation. The RMS of $\sigma(\Delta T_a)_{gl}$ is given by $\sqrt{\sum_{m=1}^{M^{TPX}} (\sigma(\Delta T_a)_{gl})^2 / M^{TPX}}$, where m is the month number and M is the number of months in TPX (either TP1 or TP2). This quantity is computed for each ATMS and AMSU-A instrument separately for TP1 and TP2 and is shown in Fig. 11A, B, respectively. These figures show comparable RMS of $\sigma(\Delta T_a)_{gl}$ from TP1 to TP2 for ATMS(AMSU-A) Ch 5(4) to Ch 11(10). The RMS of $\sigma(\Delta T_a)_{gl}$ data from all instruments cluster together for a given channel within about 0.05 K. On average, they range in value between about 0.5 K to 0.7 K. For all other channels, there are noticeable increases in RMS of $\sigma(\Delta T_a)_{gl}$ from TP1 to TP2. For the ATMS(AMSU-A) Ch 12(11) to Ch 15(14), the RMS of $\sigma(\Delta T_a)_{gl}$ increases in range from between 1.25 K and 2 K to about 1.5 K to 3.0 K from TP1 to TP2. These increases in uncertainty may be associated with regional and diurnal ionospheric variability that may impact the COSMIC-2 soundings

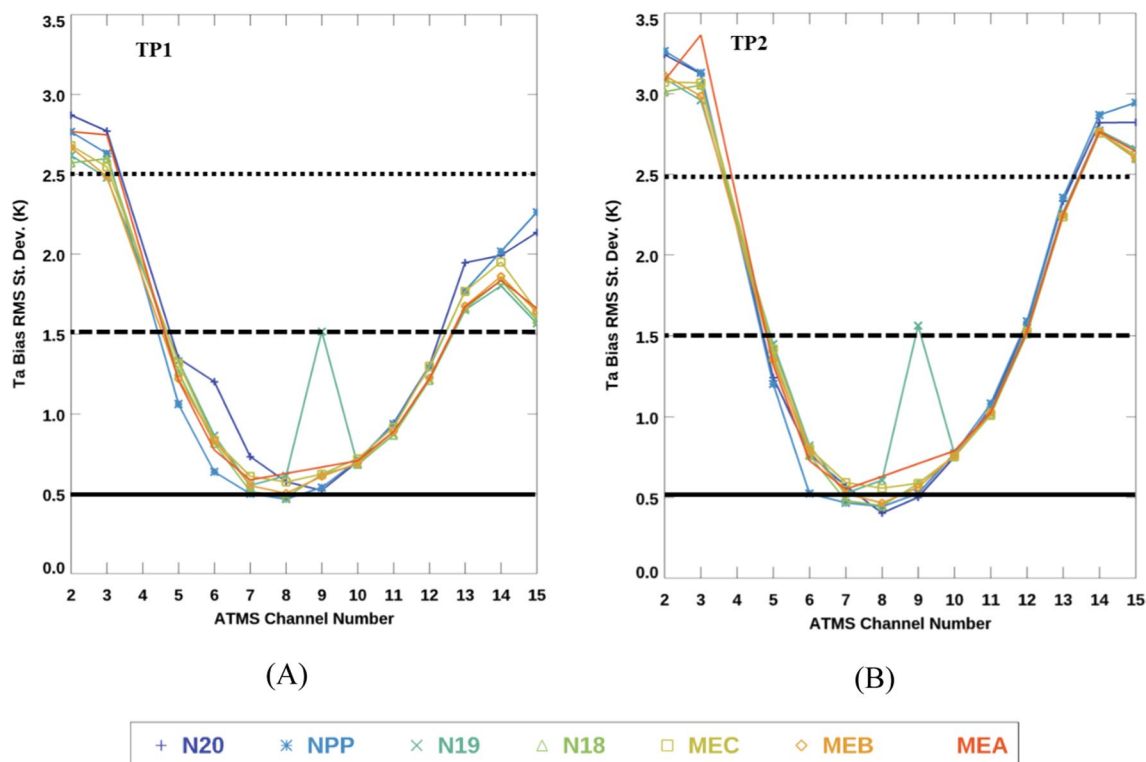


Fig. 11 The RMS of $\sigma(\Delta T_a)_{gl}$ over (A) TP1 and (B) TP2 for N18, N19, MEA, MEB, and MEC AMSU-A, and NPP and N20 ATMS are plotted for each ATMS channel. Except for ATMS Ch 2 and Ch 3, the corresponding AMSU-A channel is the ATMS channel number minus one. The three black horizontal lines are added only to facilitate the visualization change between the plots

above 40 km. Meanwhile, for ATMS and AMSU-A Ch 2 and Ch 3, the RMS of $\sigma(\Delta T_a)_{gl}$ increases from about 2.6 K to 3.1 K from TP1 to TP2. This may be related to the augmented abundance of COSMIC-2 soundings in the tropics and subtropics (see Fig. 4A), which would impact the uncertainties related to GNSS RO temperatures due to much increased integrated water vapor contents compared to mid-latitude regions.

One prominent feature visible in Fig. 11A, B is the RMS of $\sigma(\Delta T_a)_{gl}$ value of 1.5 K for N19 AMSU-A Ch 8. This outlier caused by instrument gain anomalies was discussed briefly in Sect. 4.2 and in more detail in Iacovazzi et al. (2020). Another apparent anomaly is associated with the larger RMS of $\sigma(\Delta T_a)_{gl}$ values for N20 ATMS Ch 6 and 7 for the pre-COSMIC-2 integration period, TP1. The beginning of the N20 record (the first two months) was particularly noisy, and the $\sigma(\Delta T_a)_{gl}$ values were about 5–6 K. The $\sigma(\Delta T_a)_{gl}$ values subsequently settled down to 0.5–1.0 K.

4.4 Inter-sensor monthly, TP1 and TP2 global $\mu(\delta T_a)$ statistics

Since their inception, MW satellite instruments have been critical in improving NWP (English et al. 2000; McNally et al. 2000) and creating long-term mid-tropospheric temperature climate time series (Zou et al. 2018; Wang and Zou 2006; Spencer et al. 2006; Mears et al. 2003; Prabhakara et al. 2000). Such projects have revealed that inherent calibration-related Tb biases and bias trends between operating MW instruments must be detected and corrected, or they could lead to significant errors in weather forecasts and climate products. In addition, with proposed future SmallSat and CubeSat MW radiometers, establishing a calibration link between these radiometers and the more established AMSU-A and ATMS MW instruments is critical in ensuring continuity of data used for NWP and long-term climate change analyses.

It is possible to use the global monthly-mean O-B Ta bias, $\mu(\Delta T_a)_{gl}$, statistics generated with the help of the RO soundings and CRTM to determine and analyze inter-sensor monthly-mean Ta biases, $\mu(\delta T_a)_{gl}$. This is accomplished by assuming that the CRTM-simulated AMSU-A and ATMS Tb data generated using the RO soundings represent a reference standard that has uniform performance relative to all sensors. Then, when the $\mu(\Delta T_a)_{gl}$ values of one operational sensor are subtracted from those of another operational sensor, the CRTM-simulated values are assumed to be factored out to produce an estimate of $\mu(\delta T_a)_{gl}$. So, simply subtracting the $\mu(\Delta T_a)_{globe}$ values for different instruments during their

periods of operational overlap establishes “double-difference” sensor-to-sensor $\mu(\delta T_a)_{gl}$ statistics.

For N18, N19, MEA, MEB, and MEC AMSU-A and NPP and N20 ATMS units, there are 10 AMSU-A-to-AMSU-A, 10 ATMS-to-AMSU-A, and 1 ATMS-to-ATMS instrument pair(s) possible, where each pair can produce inter-sensor $\mu(\delta T_a)_{gl}$ values using the double difference. To avoid overcrowding the graphical representation of these results, the double-difference analysis is simplified. For a given MW sounder channel, the minimum and maximum of the set of 10 AMSU-A-to-AMSU-A inter-sensor $\mu(\delta T_a)_{gl}$ values from a single month are determined and stored. This is repeated for all months for that channel. This process can be mathematically expressed with set-builder notation for a given AMSU-A channel and for each month as follows:

$$[\mu(\delta T_a)_{gl}]_{Min}(m) = MIN \left\{ [\mu(\Delta T_a)_{gl}]_{m,j} - [\mu(\Delta T_a)_{gl}]_{m,i} \mid j > i, i = 1 : 4 \text{ and } j = 1 : 5 \right\},$$

$$[\mu(\delta T_a)_{gl}]_{Max}(m) = MAX \left\{ [\mu(\Delta T_a)_{gl}]_{m,j} - [\mu(\Delta T_a)_{gl}]_{m,i} \mid j > i, i = 1 : 4 \text{ and } j = 1 : 5 \right\}.$$

In these equations, $[\mu(\Delta T_a)_{gl}]_{m,j}$ is the monthly-mean O-B Ta bias for a given channel, and m is the month number given M^{TPX} months in the time period. The double difference and minimum and maximum statistics yield values that represent the minimum or maximum inter-sensor $\mu(\delta T_a)_{gl}$ for a given channel for a given month. The variable $i=1:4$ represents the N18, N19, MEA, and MEB AMSU-A units, and $j=1:5$ includes these AMSU-A units and MEC AMSU-A. A similar computational procedure can be applied to the ATMS-to-AMSU-A instrument pairs and separately to the ATMS-to-ATMS instrument pair. The ATMS-to-ATMS $[\mu(\delta T_a)_{gl}]_{Min}(m)$ and $[\mu(\delta T_a)_{gl}]_{Max}(m)$ values are equal since there is only one pair of ATMS instruments. Time series of $[\mu(\delta T_a)_{gl}]_{Min}(m)$ and $[\mu(\delta T_a)_{gl}]_{Max}(m)$ values for ATMS and AMSU-A Ch 2, ATMS(AMSU-A) Ch 10(9), and ATMS(AMSU-A) Ch 15(14) can be seen in Fig. 12A–C, respectively.

Figure 12A clearly shows that introducing COSMIC-2 data in TP2 stabilizes the inter-sensor Ta bias statistics. In this figure, the variability from month to month visible in TP1 becomes very small in TP2. A similar result is found in Fig. 12C, except for slight synchronized variations in the minimum and maximum values are found between ATMS-to-AMSU double differences. Figure 12B shows very little change between TP1 and TP2 minimum and maximum double difference values for ATMS(AMSU-A) Ch 10(9). This attests to the relatively low uncertainties

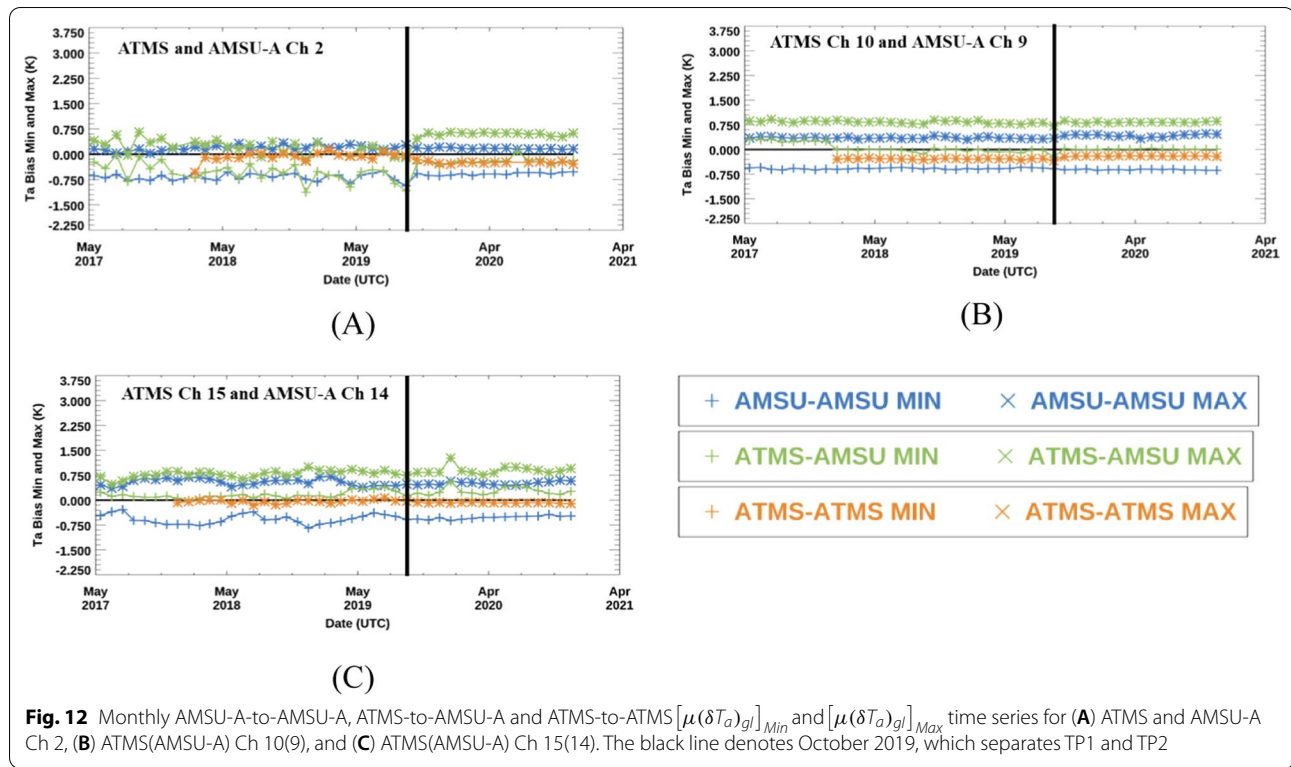


Fig. 12 Monthly AMSU-A-to-AMSU-A, ATMS-to-AMSU-A and ATMS-to-ATMS $[\mu(\delta T_a)_{gl}]_{Min}$ and $[\mu(\delta T_a)_{gl}]_{Max}$ time series for (A) ATMS and AMSU-A Ch 2, (B) ATMS(AMSU-A) Ch 10(9), and (C) ATMS(AMSU-A) Ch 15(14). The black line denotes October 2019, which separates TP1 and TP2

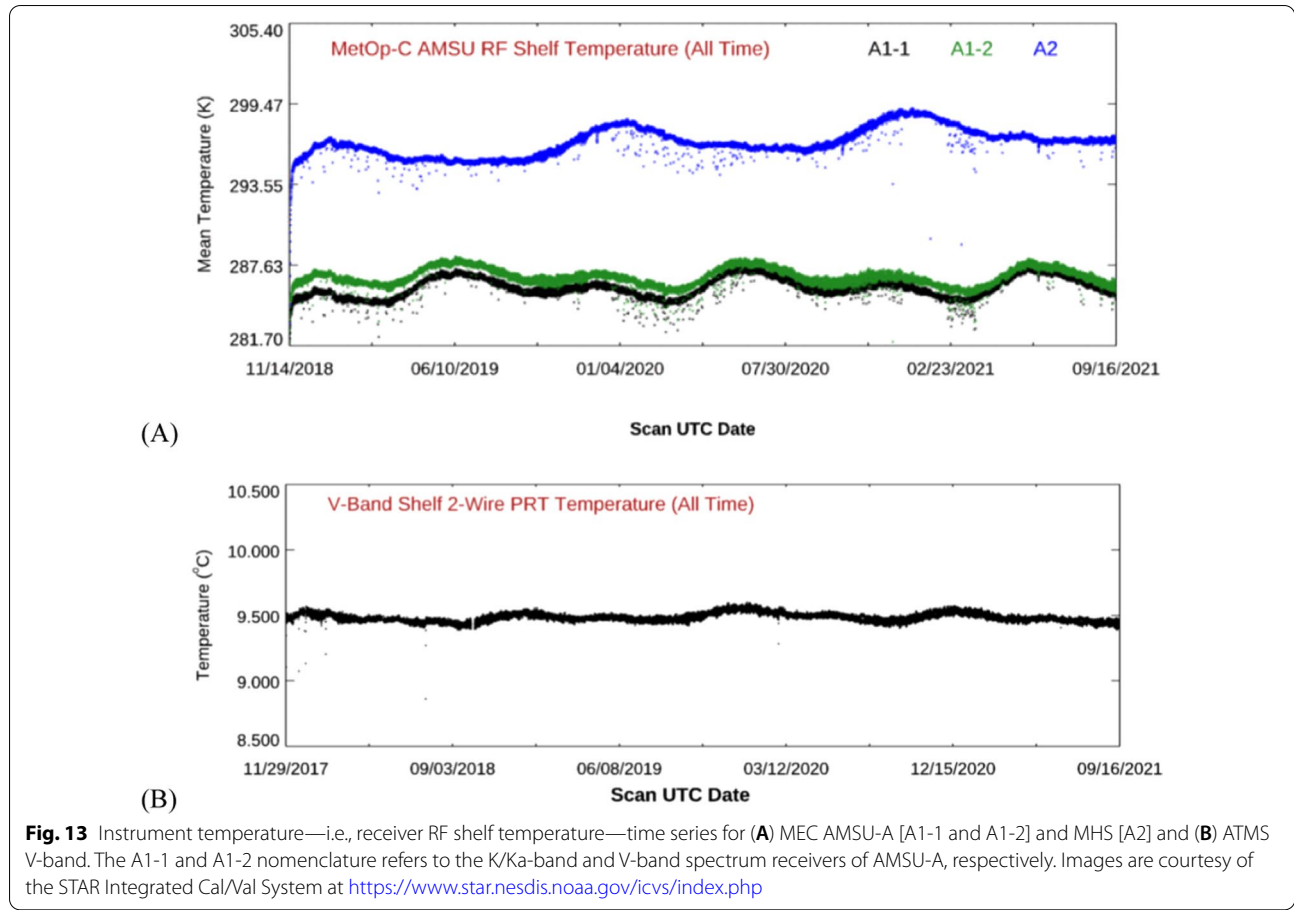
of the RO soundings and weak Ta gradients in the earth scenes for this channel.

There are at least two possible explanations for the variation found in Fig. 12C. It may be due to differences in the ATMS and AMSU-A calibration procedures. For example, the ATMS data processing algorithm contains an important correction for non-zero antenna reflector emissivity that has not been applied to the AMSU-A instruments. Since this correction depends on the thermal state of a microwave instrument, this could create a seasonal variability between ATMS and AMSU-A data. Figure 13A, B show the lifetime instrument temperature timeseries for N20 ATMS and MEC AMSU-A. This shows annual swings of ATMS instrument temperature are less than 0.1 K, while for AMSU-A they are as large as 3 K. The uncorrected reflector emissivity in AMSU-A could be responsible for seasonal bias variations between ATMS and AMSU-A.

One alternative explanation for this semi-annual behavior is that polar-orbiting N20 and NPP ATMS have “afternoon-orbit” local equatorial crossing times (LECTs) of 1:30 am/pm, and all the AMSU-A instruments have LECTs closer to a 6 am/pm terminator orbit. For example, the current operational AMSU-A instrument LECT orbit times are as follows: N18 (10 am/pm), N19 (3:30 am/pm), MEA (8 am/pm), MEB (9:30 am/pm), and MEC (9:30 am/pm). The LECT is the local time of day

at satellite nadir as the spacecraft orbit crosses the equator. This LECT represents earth scene local time of day to within about 1 h for all latitudes stretching from 60°S to 60°N. The climatological change in ionospheric total electron content signal may be different depending on the time of day, which may leave some residual signal left over in the double difference results between ATMS and AMSU-A instruments. Further study that is beyond the scope of this paper is needed to reach any conclusions.

The results in Fig. 12C are significant in the fact that the large semi-annual variations in $\mu(\Delta T_a)_{gl}$ time-series values shown in Fig. 10A do not translate into noisy values of the inter-satellite $\mu(\delta T_a)_{gl}$ values computed using the double difference. This uncovers the usefulness of RO data to support MW inter-sensor bias monitoring, even when the GNSS RO soundings above 40 km may contain time-dependent temperature biases that manifest as systematic individual ATMS and AMSU-A instrument $\mu(\Delta T_a)_{gl}$ time-series variations. Figure 12A can be used to reach a similar conclusion for surface-sensitive MW channels that depend on the lower-reaches of the GNSS RO soundings. In Fig. 12A, C, the COSMIC-2 driven TP2 inter-sensor $\mu(\delta T_a)_{gl}$ results are more stable than the pre-COSMIC-2 TP1 results. This indicates that a sufficient number of RO data samples are needed to establish double-difference analysis stability for these MW channels. The relatively stable Fig. 12B results help draw



the conclusion that much fewer RO samples are needed to establish stable MW inter-sensor T_a bias monitoring for ATMS(AMSU-A) Chs 6–11(5–10). These channels have weighting function peaks within the high-accuracy 8–30 km portions of the RO temperature and moisture soundings, and this altitude range has much reduced earth scene T_a gradients.

The existing AMSU-A-to-AMSU-A, ATMS-to-AMSU-A and ATMS-to-ATMS monthly $[\mu(\delta T_a)_{gl}]_{Min}$ and $[\mu(\delta T_a)_{gl}]_{Max}$ time series values can be separately averaged over TP1 and TP2 to generate TP1- and TP2-mean minimum and maximum inter-sensor T_a biases, $\mu[\mu(\delta T_a)_{gl}]_{Min}^{TP1}$, $\mu[\mu(\delta T_a)_{gl}]_{Max}^{TP1}$, $\mu[\mu(\delta T_a)_{gl}]_{Min}^{TP2}$ and $\mu[\mu(\delta T_a)_{gl}]_{Max}^{TP2}$. For a given channel this translates to the following equations:

$$\mu[\mu(\delta T_a)_{gl}]_{Min}^{TPX} = \frac{1}{M^{TPX}} \sum_{m=1}^{M^{TPX}} (\mu(\delta T_a)_{gl}^{Min}(m)) \text{ and}$$

$$\mu[\mu(\delta T_a)_{gl}]_{Max}^{TPX} = \frac{1}{M^{TPX}} \sum_{m=1}^{M^{TPX}} (\mu(\delta T_a)_{gl}^{Max}(m)).$$

In these equations, TPX can be either TP1 or TP2. This analysis can be carried out for all channels, and performed for AMSU-A-to-AMSU-A, ATMS-to-AMSU-A and ATMS-to-ATMS minimum and maximum monthly inter-sensor $\mu(\delta T_a)_{gl}$ values. Figure 14A shows the $\mu[\mu(\delta T_a)_{gl}]_{Min}^{TP1}$ and $\mu[\mu(\delta T_a)_{gl}]_{Max}^{TP1}$ results for the AMSU-A-to-AMSU-A, ATMS-to-AMSU-A and ATMS-to-ATMS double difference populations. Figure 14B presents the same plot, except using $\mu[\mu(\delta T_a)_{gl}]_{Min}^{TP2}$ and $\mu[\mu(\delta T_a)_{gl}]_{Max}^{TP2}$ values computed for TP2. The differences between $\mu[\mu(\delta T_a)_{gl}]_{Min}^{TP2}$ and $\mu[\mu(\delta T_a)_{gl}]_{Min}^{TP1}$ ($\mu[\mu(\delta T_a)_{gl}]_{Min}^{TP2-TP1}$), and separately between $\mu[\mu(\delta T_a)_{gl}]_{Max}^{TP2}$ and $\mu[\mu(\delta T_a)_{gl}]_{Max}^{TP1}$ ($\mu[\mu(\delta T_a)_{gl}]_{Max}^{TP2-TP1}$), are given in Fig. 14C for

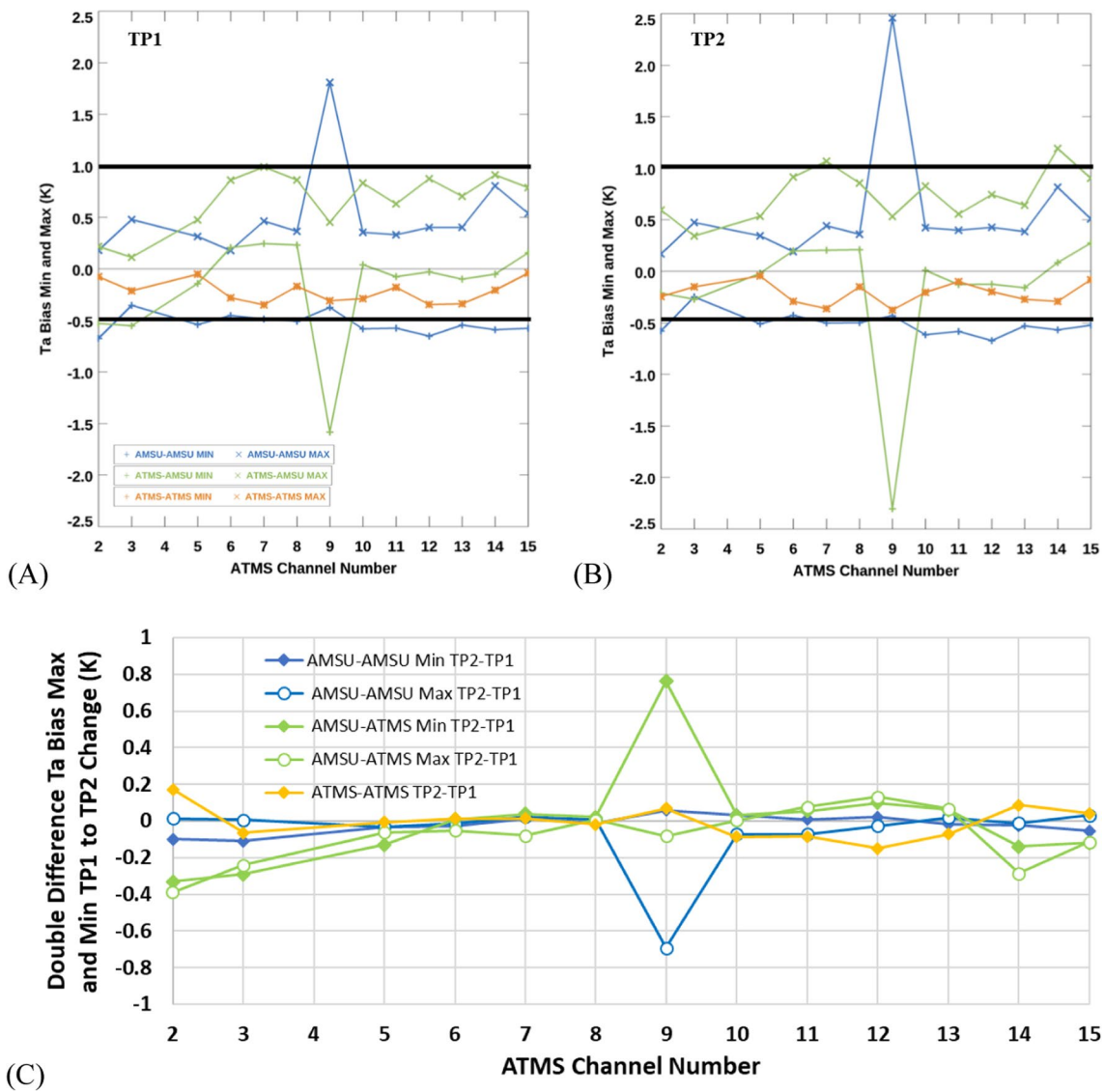


Fig. 14 The AMSU-A-to-AMSU-A, ATMS-to-AMSU-A, and ATMS-to-ATMS (A) $\mu \left[\left[\mu(\delta T_a)_{gl} \right]_{Min}^{TP1} \right]$ and $\mu \left[\left[\mu(\delta T_a)_{gl} \right]_{Max}^{TP1} \right]$, (B) $\mu \left[\left[\mu(\delta T_a)_{gl} \right]_{Min}^{TP2} \right]$ and $\mu \left[\left[\mu(\delta T_a)_{gl} \right]_{Max}^{TP2} \right]$, and (C) $\mu \left[\left[\mu(\delta T_a)_{gl} \right]_{Min}^{TP2-TP1} \right]$ and $\mu \left[\left[\mu(\delta T_a)_{gl} \right]_{Max}^{TP2-TP1} \right]$. Note that except for ATMS Ch 2 and Ch 3, the corresponding AMSU-A channel is the ATMS channel number minus one. The black horizontal lines in A are included to simply capture the bulk range of the data

AMSU-A-to-AMSU-A, ATMS-to-AMSU-A, and ATMS-to-ATMS.

Figure 14C shows for all channels that the absolute value of TP1 to TP2 change is less than about 0.4 K except N19 Ch 8, which has notably unstable channel performance between TP1 and TP2. As foreshadowed by Fig. 12B, the ATMS(AMSU-A) sounding channels from Chs 5–11(4–10) have the least differences between TP1 and TP2 (<0.1 K). This is because GNSS RO soundings are known to have the least uncertainties

between 8 and 30 km, and these MW sounder channels have significant radiometric contributions from this atmospheric layer. The $\mu \left[\left[\mu(\delta T_a)_{gl} \right]_{Min}^{TP2-TP1} \right]$ and $\mu \left[\left[\mu(\delta T_a)_{gl} \right]_{Max}^{TP2-TP1} \right]$ ranges between -0.08 K to 0.13 K in Fig. 14C when NOAA 19 Ch 8 results are ignored. These TP1 to TP2 changes are expected to be relatively minor since long-term average inter-satellite performance of MW sounders usually does not drift or vary appreciably over time in the absence of instrument

deterioration or significant data processing algorithms changes. Since inter-sensor $\mu(\delta T_a)_{gl}$ values in this analysis are preserved for MW sounding channels with weighting function peaks in the low-troposphere to low-stratosphere, COSMIC-2 is shown to competently continue support of long-term GNSS RO soundings-based MW data monitoring for these channels.

The larger $\mu[\mu(\delta T_a)_{gl}]_{Min}^{TP2-TP1}$ and $\mu[\mu(\delta T_a)_{gl}]_{Max}^{TP2-TP1}$ shifts seen in Fig. 14C for the other MW sounder channels can be explained by GNSS RO data sample population augmentation and latitudinal distribution changes after COSMIC-2 soundings are added. Radio occultation data coverage late in TP1 is limited mainly to mid-latitude regions, while in TP2 it is concentrated in the tropics and subtropics. This may skew $\mu(\delta T_a)_{gl}$ statistics due to latitudinal-dependent surface emissivity spatial variation impacts on ATMS and AMSU-A Chs 2–3 analysis, and latitudinal-dependent radiometric contributions from the lower ionosphere (>40 km) on ATMS(AMSU-A) Chs 12–15(11–14) analysis. These effects are described in more detail in Sect. 4.3, which exposed the need to have GNSS RO data that have populations that are robust *and* latitudinally stable over time to ensure stable single sensor T_a bias statistics for ATMS and AMSU-A Chs 2–3 and ATMS(AMSU-A) Chs 12–15(11–14). In Fig. 14C, one distinct feature of AMSU-A-to-AMSU-A $\mu[\mu(\delta T_a)_{gl}]_{Min}^{TP2-TP1}$ and $\mu[\mu(\delta T_a)_{gl}]_{Max}^{TP2-TP1}$ shifts is that they are within 0.1 K for these channels. This is reflected for the most part in the ATMS-to-AMSU-A changes as well. This reveals the important finding that GNSS RO soundings between the surface and 8 km, and between 30 and 60 km, have value in monitoring MW sounder inter-sensor $\mu(\delta T_a)_{gl}$ statistics. This value exists even if there are shifts in the latitudinal distribution of GNSS RO data sample population.

5 Conclusion

The June 25, 2019 launch of the COSMIC-2 GNSS RO microsatellites commenced the follow-on program to the highly successful COSMIC-1 GNSS RO Program. GNSS RO-based temperature and moisture soundings represent a tremendous boon to weather forecasting, climate monitoring, and space weather research. Also, due to their high measurement stability, the GNSS RO soundings have been utilized to monitor long-term NOAA operational MW sounding instrument product data quality. Ironically, with the highly distinct transition to using mainly COSMIC-2 sounding data on October 1, 2019, these monitoring long-term time series can

reveal, and be used to characterize, noticeable differences of simulated T_b values generated after the COSMIC-2 atmospheric soundings are implemented along with predecessor COSMIC-1 and KOMPSAT-5 Program soundings. The COSMIC-2 RO soundings impact on long-term MW sounder data monitoring can be determined from this information.

This study reveals an order of magnitude augmentation in data samples per month—from the order of 10^4 to 10^5 —after integrating COSMIC-2 soundings into the analysis. The data analysis screening and collocation processes presented in Sect. 3 reduce the number of GNSS RO soundings available for comparison with MW radiometer data by more than 85% for channels largely influenced by surface radiation and 50% for channels that are not. Data augmentation in TP2 resulting from COSMIC-2 maximizes between 2500 to 7000 samples per month near the equator, and falls to less than 300 samples per month between 40° to 50° . Poleward of 50° , attrition of COSMIC-1/KOMPSAT-5 data between TP1 and TP2 causes average decreases in monthly sample number. This represents a significant change in the latitudinal distribution of GNSS RO and MW matched samples from TP1 to TP2. In TP1 there are about 150–300% more mid-latitude than tropical GNSS RO and MW satellite data matched samples per month, while in TP2, the mid-latitudes typically have only 10% of the tropical GNSS RO and MW matched samples per month.

ATMS(AMSU-A) Ch 2, 3, and 5–6(2–5) show decreased $\mu(\Delta T_a)_{gl}$ time series standard deviation after COSMIC-2 data are added to the analysis in TP2. On the contrary, there can be sizable shifts in the TP1 to TP2 mean values of $\mu(\Delta T_a)_{gl}$ time series due to latitudinal variability in the contributions to these values. This may be caused by surface emissivity and water vapor content latitudinal variability that affects ATMS and AMSU-A Ch 2–3, and water vapor content latitudinal variability that affects ATMS(AMSU-A) Ch 5–9(4–8). For ATMS(AMSU-A) Ch 12–15(11–14), there are $\mu(\Delta T_a)_{gl}$ time series standard deviation increases and mean decreases from TP1 to TP2. This may be due to latitudinal variability in total electron content in the ionosphere that would affect COSMIC-2 soundings between 40 and 60 km. Note that some time series errors may also be due to the considerable drop in the number of COSMIC-1 profiles per month from 2017 to 2019. These issues with atmospheric sounding data between 40 and 60 km reveal limitations of tracking and trending ATMS(AMSU-A) Chs 12–15(11–14) T_a data for individual MW instruments.

There is very little change in min and max inter-sensor $\mu(\delta T_a)_{gl}$ for ATMS(AMSU-A) Ch 5–11(4–10) between TP1 to TP2. Min and max inter-sensor $\mu(\delta T_a)_{gl}$

between TP1 and TP2 become more stable in TP2 for ATMS(AMSU-A) Chs 2, 3 and 12–15(2, 3, and 11–14), but there are noticeable shifts in the overall value of min and max inter-sensor $\mu(\delta T_a)_{gl}$ between the time periods. Of particular interest is that ATMS(AMSU-A) Chs 12–15(11–14) are surprisingly flat in TP2 with the larger sample, even though COSMIC-2 data between 40 and 60 km have increased uncertainty that may be due to ionospheric contamination. In addition, these “double-difference” inter-sensor $\mu(\delta T_a)_{gl}$ statistics revealed possible difference in calibration behavior between ATMS and AMSU-A instruments, or time-of-day-dependent climatological ionospheric effects. Further work is needed to resolve this.

In this study, the COSMIC-2 data help to reveal optimization requirements for the RO-sounding-based NOAA operational MW sounding instrument product quality monitoring system. These requirements include monthly RO sounding populations that are large enough to create robust mean and standard deviation statistics. They also include RO sounding data relative distributions between latitude bands that are preserved over time to minimize shifts in the $\mu(\Delta T_a)_{gl}$ values and their long-term statistics. This is because these biases are subject to latitudinal and time-dependent variabilities in surface temperature and emissivity, water vapor column below 8 km, and/or changes in the total electron content above 40 km that affect blended ECMWF and GNSS RO sounding profiles used for CRTM Tb simulations. This study also finds that the stability of inter-sensor $\mu(\delta T_a)_{gl}$ values deduced from double differences of the individual sensor $\mu(\Delta T_a)_{gl}$ values benefit from the larger COSMIC-2 sounding population. Also, seasonal variability that may be present in individual sensor $\mu(\Delta T_a)_{gl}$ values may be largely removed in the inter-sensor $\mu(\delta T_a)_{gl}$ values after $\mu(\Delta T_a)_{gl}$ double-difference computations. This is especially relevant in ATMS(AMSU-A) Chs 12–15(11–14).

This demonstrates that the COSMIC-2 soundings provide a high-quality data continuity needed to augment sounding populations from former GNSS RO program assets. Given this success, the voluminous COSMIC-2 data may allow for expanded analyses in the future. These expanded analyses could probe into scan-angle-dependent ΔT_a values. The COSMIC-2 data could also perform a more defined analysis over different hours of the day and/or geographic regions from 40°S to 40°N. Future updates in MW sensor calibration processing may also be analyzed with the help of COSMIC-2 data. Finally, this study supports the need for the long-term continuity of GNSS RO sensors and improved sounding retrieval methods below 8 km and above 30 km.

Acknowledgements

The authors would like to thank the STAR agency and TAO journal peer reviewers for their careful reviews, which have improved the quality of the

manuscript substantially. They would also like to acknowledge the COSMIC Data Analysis and Archive Center for providing the COSMIC-1 and KOMPSAT-5 wetPrf soundings used in this study, as well as the JPSS Program for funding support of this work.

Disclaimer

The manuscript contents are solely the authors' opinions and do not constitute a statement of policy, decision, or position on behalf of NOAA or the U. S. Government.

Author's contributions

All authors read and approved the final manuscript.

Declarations

Competing interests

All authors declare no competing interest.

Author details

¹GST, Inc., 7501 Greenway Center Drive, Suite 1100, Greenbelt, MD 20770, USA.

²NOAA/NESDIS/STAR, 5830 University Research Court, College Park, MD 20740, USA.

Received: 28 January 2022 Accepted: 14 March 2022

Published online: 29 March 2022

References

- Anthes RA et al (2008) The COSMIC/FORMOSAT-3 mission: early results. *Bull Am Met Soc* 89:313–333
- Bean BR, Dutton EJ (1966) Radio meteorology. U.S. Govt. Print. Office, pp 435
- Biondi R, Randel W, Ho S-P, Neubert T, Syndergaard S (2012) Thermal structure of intense convective clouds derived from GPS radio occultations. *Atmos Chem Phys*. <https://doi.org/10.5194/acp-12-5309-2012>
- Biondi R, Ho S-P, Randel W, Neubert T, Syndergaard S (2013) Tropical cyclone cloud-top heights and vertical temperature structure detection using GPS radio occultation measurements. *J Geophys Res* 118:1–13. <https://doi.org/10.1002/jgrd.50448>
- English SJ, Renshaw RJ, Dibben PC, Smith AJ, Rayer PJ, Poulsen C, Saunders FW, Eyre JR (2000) A comparison of the impact of TOVS and ATOVS satellite sounding data on the accuracy of numerical weather forecasts. *Q J Royal Met Soc* 126:2911–2931
- Grody N, Zhao J, Ferraro R, Weng F, Boers R (2001) Determination of precipitable water and cloud liquid water over oceans from the NOAA 15 advanced microwave sounding unit. *J Geophys Res* 106(D3):2943–2953
- Han Y, Weng F, Zou X, Yang H, Scott D (2016) Characterization of geolocation accuracy of Suomi NPP Advanced Technology Microwave Sounder measurements. *J Geophys Res Atmos* 121:4933–4950. <https://doi.org/10.1002/2015JD024278>
- Healy S, Eyre J (2000) Retrieving temperature, water vapor and surface pressure information from refractivity-index profiles derived by radio occultation: a simulation study. *Q J Royal Met Soc* 126:1661–1683
- Ho S-P et al (2009) Calibration of temperature in the lower stratosphere from microwave measurements using COSMIC radio occultation data: Preliminary results. *Terr Atmos Ocean Sci* 20:87. [https://doi.org/10.3319/TAO.2007.12.06.01\(F3C\)](https://doi.org/10.3319/TAO.2007.12.06.01(F3C))
- Ho S-P, Zhou X, Kuo Y-H, Hunt D, Wang J-H (2010) Global evaluation of radio-sonde water vapor systematic biases using GPS radio occultation from COSMIC and ECMWF analysis. *Remote Sens* 2:1320–1330
- Ho S-P, Kuo Y-H, Schreiner W, Zhou X (2010b) Using SI traceable global positioning system radio occultation measurements for climate monitoring, in: states of the climate in 2009. *Bull Am Met Soc* 91:S36–S37
- Ho S-P, Yue X, Zeng Z, Ao C, Huang C-Y, Kursinski ER, Kuo Y-H (2013) Applications of COSMIC radio occultation data from the troposphere to ionosphere and potential impacts of COSMIC-2 data. *Bull Am Met Soc Bull*. <https://doi.org/10.1175/BAMS-D-13-00035.1>
- Ho S-P et al (2015) Marine boundary layer heights and their longitudinal, diurnal, and inter-seasonal variability in the Southeastern Pacific using

- COSMIC, CALIOP, and radiosonde data. *J Clim* 28:2856–2872. <https://doi.org/10.1175/JCLI-D-14-00238.1>
- Ho S-P, Peng L, Voemel H (2017) Characterization of the long-term radiosonde temperature biases in the upper troposphere and lower stratosphere using COSMIC and MetOp-A/GRAS data from 2006 to 2014. *Atmos Chem Phys* 17:4493–4511. <https://doi.org/10.5194/acp-17-4493-2017>
- Ho S-P, Peng L, Mears C, Anthes RA (2018) Comparison of global observations and trends of total precipitable water derived from microwave radiometers and COSMIC radio occultation from 2006 to 2013. *Atmos Chem Phys* 18:259–274. <https://doi.org/10.5194/acp-18-259-2018>
- Ho S-P, Zhou X, Shao X, Zhang B, Adhikari L, Kireev S, He Y, Yoe JG, Xia-Serafino W, Lynch E (2020) Initial Assessment of the COSMIC-2/FORMOSAT-7 neutral atmosphere data quality in NESDIS/STAR using in situ and satellite data. *Remote Sens* 12:4099
- Ho SP et al. (2021) NESDIS STAR GNSS RO Processing, Validation, and Monitoring System: Quality Assessment Results for COSMIC-2, TAO (submitted)
- Huang C-Y, Teng WH, Ho S-P, Kuo YH (2013) Global variation of COSMIC precipitable water over land: comparisons with ground-based GPS measurements and NCEP reanalyses. *Geophys Res Lett*. <https://doi.org/10.1002/grl.50885>
- Iacovazzi R, Lin L, Sun N, Liu Q (2020) NOAA operational microwave sounding radiometer data quality monitoring and anomaly assessment using COSMIC GNSS radio-occultation soundings. *Remote Sens* 12(5):828
- Kireev S, Ho S-P, Zhou X (2020) The Development of COSMIC-2 Temperature, Moisture, and Pressure Retrieval Algorithm at NOAA/STAR. In: 5th International Conference on GPS Radio Occultation, Hsinchu, Taiwan (Poster @ <http://w3.nspo.narl.org.tw/ICGPSRO2020/download/poster/ICGPSRO2020-presentation-AB028-T73j6waN95.pdf>)
- Kishore P, Namboothiri SP, Jiang JH, Sivakumar V, Igarashi K (2008) Global temperature estimates in the troposphere and stratosphere: a validation study of COSMIC/FORMOSAT-3 measurements. *Atmos Chem Phys Discuss* 8:8327–8355
- Lean JL, Meier RR, Picone JM, Sassi F, Emmert JT, Richards PG (2016) Ionospheric total electron content: spatial patterns of variability. *J Geophys Res Space Physics* 121:10367–10402. <https://doi.org/10.1002/2016JA023210>
- Liu Q, Boukabara S (2014) Community radiation transfer model (CRTM) applications in supporting the Suomi national polar-orbiting partnership (SNPP) mission validation and verification. *Remote Sens Environ* 140:744–754
- McNally AP, Derber JC, Wu W-S, Katz BB (2000) The use of TOVS level-1 radiances in the NCEP SSI analysis system. *Q J Royal Met Soc* 129:689–724
- Mears C, Schabel M, Wentz F (2003) A reanalysis of the MSU Channel 2 tropospheric temperature record. *J Climate* 16:3650–3664
- Mears C et al (2019) Total column water vapor, [In “States of the Climate in 2018”. *Bull Am Met Soc* 100(9):S24–S25. <https://doi.org/10.1175/2019BAMSStateoftheClimate.1>
- Mears C, Ho S-P, Wang J, Huelsing H, Peng L (2020) Total column water vapor, [In “States of the Climate in 2019”. *Bull Am Met Soc* 101(8):S24–S25. <https://doi.org/10.1175/2019BAMSStateoftheClimate>
- Palmer PI, Barnett J, Eyre J, Healy S (2000) A non-linear optimal estimation inverse method for radio occultation measurements of temperature, humidity, and surface pressure. *J Geophys Res* 105:17513–17526
- Prabhakara C, Iacovazzi R Jr, Yoo J-M, Dalu G (2000) Global warming: evidence from satellite observations. *Geophys Res Lett* 27(21):3517–3520
- Rieckh T, Anthes RA, Randel W, Ho S-P, Foelsche U (2017) Tropospheric dry layers in the tropical western Pacific: comparisons of GPS radio occultation with multiple data sets. *Atmos Measure Tech* 10:1093–1110. <https://doi.org/10.5194/amt-10-1093-2017>
- Scherllin-Pirscher B, Deser C, Ho S-P, Chou C, Randel W, Kuo YH (2012) The vertical and spatial structure of ENSO in the upper troposphere and lower stratosphere from GPS radio occultation measurements. *Geophys Res Lett* 39(L20801):6. <https://doi.org/10.1029/2012GL053071>
- Schröder M et al (2019) The GEWEX water vapor assessment: overview and introduction to results and recommendations. *Remote Sens* 11(3):251. <https://doi.org/10.3390/rs11030251>
- Shao X, Ho S-P, Zhang B, Zou X, Kireev S, Yong C, Cao CY (2021) Comparison of COSMIC-2 radio occultation retrieval products with Vaisala RS41 and RS92 radiosonde water vapor and upper-air temperature measurements. *Terr Atmos Ocean*
- Spencer RW, Christy JR, Braswell WD, Norris WB (2006) Estimation of tropospheric temperature trends from MSU Channels 2 and 4. *J Atmos Ocean Tech* 23:417–423
- Teng WH, Huang CY, Ho S-P, Kuo YH, Zhou XJ (2013) Characteristics of global precipitable water in ENSO events revealed by COSMIC measurements. *J Geophys Res* 118:1–15. <https://doi.org/10.1002/jgrd.50371>
- Wang W, Zou C (2014) AMSU-A-only atmospheric temperature data records from the lower troposphere to the top of the stratosphere. *J Atmos Ocean Tech* 31(4):808–825
- Weng F, Zhao L, Ferraro R, Poe G, Li X, Grody N (2003) Advanced microwave sounding unit cloud and precipitation algorithms. *Radio Sci* 38:8086–8096. <https://doi.org/10.1029/2002RS002679>
- Weng F, Zou X, Wang X, Yang S, Goldberg MD (2012) Introduction to Suomi national polar-orbiting partnership advanced technology microwave sounder for numerical weather prediction and tropical cyclone applications. *J Geophys Res* 117:D19112. <https://doi.org/10.1029/2012JD018144>
- Weng F, Zou X, Sun N, Yang H, Tian M, Blackwell WJ, Wang X, Lin L, Anderson K (2013) Calibration of Suomi national polar-orbiting partnership advanced technology microwave sounder. *J Geophys Res Atmos* 118:11187–11200. <https://doi.org/10.1002/jgrd.50840>
- Xue YH, Li J, Menzel P, Borbas E, Ho SP, Li Z (2018) Impact of sampling biases on the global trend of total precipitable water derived from the latest 10-year data of COSMIC, SSMIS and HIRS Observations. *J Geophys Res Atmos* 124(13):6966–6981
- Yang H, Weng F, Anderson K (2016) Estimation of ATMS antenna emission from cold space observations. *IEEE Trans Geosci Remote Sens* 54(8):4479–4487. <https://doi.org/10.1109/TGRS.2016.2542526>
- Yang H et al (2021) ATMS radiance data products calibration and evaluation. *IEEE Trans Geosci Remote Sens*. <https://doi.org/10.1109/TGRS.2021.3123576>
- Yu X, Xie F, Ao CO (2018) Evaluating the lower-tropospheric COSMIC GPS radio occultation sounding quality over the Arctic. *Atmos Meas Tech* 11:2051–2066. <https://doi.org/10.5194/amt-11-2051-2018>
- Zeng Z, Ho S-P, Sokolovskiy S (2012) The structure and evolution of Madden-Julian oscillation from FORMOSAT-3/COSMIC radio occultation data. *J Geophys Res* 117:D22108. <https://doi.org/10.1029/2012JD017685>
- Zou X, Vandenberghe F, Wang B, Gorbunov ME, Kuo Y-H, Sokolovskiy S, Chang JC, Sela JG, Anthes RA (1999) A ray-tracing operator and its adjoint for the use of GPS/MET refraction angle measurements. *J Geophys Res* 104(D18):22301–22318
- Zou C-Z, Goldberg MD, Cheng Z, Grody NC, Sullivan JT, Cao C, Tarpley D (2006) Recalibration of microwave sounding unit for climate studies using simultaneous nadir overpasses. *J Geophys Res* 111:D19114. <https://doi.org/10.1029/2005JD006798>
- Zou C-Z, Goldberg MD, Hao X (2018) New generation of U.S. satellite microwave sounder achieves high radiometric stability performance for reliable climate change detection. *Sci Adv* 4(10):eaau0049. <https://doi.org/10.1126/sciadv.aau0049>

Publisher's Note

Springer Nature remains neutral with regard to jurisdictional claims in published maps and institutional affiliations.

Submit your manuscript to a SpringerOpen[®] journal and benefit from:

- Convenient online submission
- Rigorous peer review
- Open access: articles freely available online
- High visibility within the field
- Retaining the copyright to your article

Submit your next manuscript at ► [springeropen.com](https://www.springeropen.com)